

NUSTAR SPECTROSCOPY OF MULTI-COMPONENT X-RAY REFLECTION FROM NGC 1068

FRANZ E. BAUER,^{1,2,3,4} PATRICIA ARÉVALO,^{5,3} DOMINIC J. WALTON,⁶ MICHAEL J. KOSS,^{7,8} SIMONETTA PUC CETTI,^{9,10} POSHAK GANDHI,¹¹ DANIEL STERN,⁶ DAVID M. ALEXANDER,¹² MISLAV BALOKOVIĆ,¹³ STEVE E. BOGGS,¹⁴ WILLIAM N. BRANDT,^{15,16} MURRAY BRIGHTMAN,¹³ FINN E. CHRISTENSEN,¹⁷ ANDREA COMASTRI,¹⁸ WILLIAM W. CRAIG,^{14,19} AGNESE DEL MORO,¹² CHARLES J. HAILEY,²⁰ FIONA A. HARRISON,¹³ RYAN HICKOX,²¹ BIN LUO,¹⁵ CRAIG B. MARKWARDT,²² ANDREA MARINUCCI,²³ GIORGIO MATT,²³ JANE R. RIGBY,²² ELIZABETH RIVERS,¹³ CRISTIAN SAEZ,²⁴ EZEQUIEL TREISTER,^{25,3} C. MEGAN URRY,²⁶ AND WILLIAM W. ZHANG.²²

The Astrophysical Journal (submitted, 11/03/14)

ABSTRACT

We report on observations of NGC 1068 with *NuSTAR*, which provide the best constraints to date on its > 10 keV spectral shape. The *NuSTAR* data are consistent with past instruments, with no strong continuum or line variability over the past two decades, consistent with its classification as a Compton-thick AGN. The combined *NuSTAR*, *Chandra*, *XMM-Newton*, and *Swift* BAT spectral dataset offers new insights into the complex secondary emission seen instead of the completely obscured transmitted nuclear continuum. The critical combination of the high signal-to-noise *NuSTAR* data and the decomposition of the nuclear and extranuclear emission with *Chandra* allow us to break several model degeneracies and greatly aid physical interpretation. When modeled as a monolithic (i.e., a single N_{H}) reflector, none of the common Compton-reflection models are able to match the neutral fluorescence lines and broad spectral shape of the Compton reflection without requiring unrealistic physical parameters (e.g., large Fe overabundances, inconsistent viewing angles, poor fits to the spatially resolved spectra). A multi-component reflector with three distinct column densities (e.g., with best-fit values of $N_{\text{H}} = 1.5 \times 10^{23}$, 5×10^{24} , and 10^{25} cm^{-2}) provides a more reasonable fit to the spectral lines and Compton hump, with near-solar Fe abundances. In this model, the higher N_{H} component provides the bulk of the flux to the Compton hump while the lower N_{H} component produces much of the line emission, effectively decoupling two key features of Compton reflection. We also find that $\approx 30\%$ of the neutral Fe $K\alpha$ line flux arises from $> 2''$ (≈ 140 pc) and is clearly extended, implying that a significant fraction of the < 10 keV reflected component arises from regions well outside of a parsec-scale torus. These results likely have ramifications for the interpretation of Compton-thick spectra from observations with poorer signal-to-noise and/or more distant objects.

Subject headings: Galaxies: active — galaxies: individual (NGC 1068) — X-rays: galaxies

¹ Pontificia Universidad Católica de Chile, Instituto de Astrofísica, Casilla 306, Santiago 22, Chile

² Millennium Institute of Astrophysics, Santiago, Chile

³ EMBIGGEN Anillo, Concepción, Chile

⁴ Space Science Institute, 4750 Walnut Street, Suite 205, Boulder, Colorado 80301

⁵ Instituto de Física y Astronomía, Facultad de Ciencias, Universidad de Valparaíso, Gran Bretaña N 1111, Playa Ancha, Valparaíso, Chile

⁶ Jet Propulsion Laboratory, California Institute of Technology, 4800 Oak Grove Drive, Pasadena, CA 91109, USA

⁷ Institute for Astronomy, Department of Physics, ETH Zurich, Wolfgang-Pauli-Strasse 27, CH-8093 Zurich, Switzerland

⁸ SNSF Ambizione Postdoctoral Fellow

⁹ ASDC-ASI, Via del Politecnico, I-00133 Roma, Italy

¹⁰ INAF-Osservatorio Astronomico di Roma, via Frascati 33, I-00040 Monte Porzio Catone (RM), Italy

¹¹ School of Physics and Astronomy, University of Southampton, Highfield, Southampton SO17 1BJ, UK

¹² Department of Physics, Durham University, South Road, Durham, DH1 3LE, UK

¹³ Cahill Center for Astronomy and Astrophysics, California Institute of Technology, Pasadena, CA 91125, USA

¹⁴ Space Sciences Laboratory, University of California, Berkeley, CA 94720, USA

¹⁵ Department of Astronomy and Astrophysics, The Pennsylvania State University, 525 Davey Lab, University Park, PA 16802, USA

¹⁶ Institute for Gravitation and the Cosmos, The Pennsylvania State University, University Park, PA 16802, USA

¹⁷ DTU Space, National Space Institute, Technical University of Denmark, Elektrovej 327, 2800 Lyngby, Denmark

¹⁸ INAF-Osservatorio Astronomico di Bologna, via Ranzani 1, I-40127 Bologna, Italy

¹⁹ Lawrence Livermore National Laboratory, Livermore, CA 945503, USA

²⁰ Columbia Astrophysics Laboratory, Columbia University, New York, NY 10027, USA

²¹ Department of Physics and Astronomy, Dartmouth College, 6127 Wilder Laboratory, Hanover, NH 03755, USA

²² NASA Goddard Space Flight Center, Greenbelt, MD 20771, USA

²³ Dipartimento di Matematica e Fisica, Università degli Studi Roma Tre, via della Vasca Navale 84, I-00146 Roma, Italy

²⁴ Department of Astronomy, University of Maryland, College Park, MD 20742, USA

²⁵ Departamento de Astronomía Universidad de Concepción, Casilla 160-C, Concepción, Chile

²⁶ Department of Physics and Yale Center for Astronomy and Astrophysics, Yale University, New Haven, CT 06520-8120, USA

1. INTRODUCTION

At a distance of ≈ 14.4 Mpc (Tully 1988), NGC 1068 is one of the nearest and best-studied Active Galactic Nuclei (AGN). It is traditionally classified as a Seyfert 2 galaxy, and was the first type 2 AGN observed to possess polarized optical broad-line emission; these broad line regions seen only in scattered light are presumably obscured by a dusty edge-on structure (a.k.a. the “torus”; Antonucci & Miller 1985; Miller et al. 1991), thereby establishing the standard orientation-based model of AGN unification as we know it today (Antonucci 1993; Urry & Padovani 1995). NGC 1068 has continued to be an exceptionally rich source for studying AGN in general and Compton-thick AGN in particular,²⁷ as there are spatially resolved studies of the AGN structure down to ≈ 0.5 – 70 pc over many critical portions of the electromagnetic spectrum ($1'' = 70$ pc at the distance of NGC 1068). In many ways, NGC 1068 is considered an archetype of an obscured AGN.

In terms of its basic properties and structure, H_2O megamaser emission coincident with the nucleus and associated with a thin disk, has constrained the supermassive black hole (SMBH) mass at the center of NGC 1068 to be $\approx 1 \times 10^7 M_\odot$ within 0.65 pc, although the observed deviations from Keplerian rotation leave some ambiguity about the overall mass distribution (e.g., Greenhill et al. 1996; Gallimore et al. 2004; Lodato & Bertin 2003). A dynamical virial mass estimate based on the width of the $\text{H}\beta$ line, $\sigma_{\text{H}\beta}$, from the scattered “polarized broad lines” in the hidden broad line region (BLR) has found a consistent mass of $(9.0 \pm 6.6) \times 10^6 M_\odot$ (e.g., Kuo et al. 2011). NGC 1068’s bolometric luminosity has been estimated to be $L_{\text{bol}} = (6\text{--}10) \times 10^{44}$ erg s^{-1} (Woo & Urry 2002; Alonso-Herrero et al. 2011) based on mid-infrared (MIR) spectral modeling assuming reprocessed AGN emission. Combined with the SMBH mass estimate, this luminosity approaches ≈ 50 – 80% of the Eddington luminosity, indicating rapid accretion.

Very Long Baseline Interferometry (VLBI) observations of the maser disk constrain it to lie between radii of 0.6 – 1.1 pc at a position angle (PA) of $\approx -45^\circ$ (east of north; e.g., Greenhill et al. 1996). At centimeter wavelengths, a weak kpc-scale, steep-spectrum radio jet is seen to extend out from the nucleus, initially at $PA = 12^\circ$ before bending to $PA = 30^\circ$ at large scales (e.g., Wilson & Ulvestad 1987; Gallimore et al. 1996). Fainter radio structures close to the nucleus are also observed to trace both the maser disk and an inner X-ray-irradiated molecular disk extending out to ≈ 0.4 pc with a $PA \approx -60^\circ$ (e.g., Gallimore et al. 2004).

At MIR wavelengths, a complex obscuring structure has been spatially resolved in NGC 1068 via Keck and VLT interferometry (e.g., Bock et al. 2000; Jaffe et al. 2004) and appears to be comprised of at least two distinct components (Raban et al. 2009; Schartmann et al. 2010). The first is a ~ 800 K, geometrically thin, disk-like structure extending ≈ 1.35 pc by 0.45 pc in size (full-width half maximum, FWHM) and aligned at $PA = -42^\circ$, which is likely associated with the maser disk. The second is a ~ 300 K, more flocculent, filamentary, torus-like distribution ≈ 3 – 4 pc in size (FWHM) which has been identified with the traditional torus. The parameters of the spectral modeling to the overall MIR light are consistent, with a torus radius of ≈ 2 pc and angular width of 26_{-4}^{+6} deg, a viewing angle of 88_{-3}^{+2} deg with

respect to the line-of-sight, and a covering factor of ≈ 25 – 40% (Alonso-Herrero et al. 2011). While no dust reverberation studies have been published on NGC 1068, the sizes from interferometry are consistent with the inner radii determined from dust reverberation studies of type 1 AGN (Suganuma et al. 2006; Koshida et al. 2014).

NGC 1068 also displays a striking extended narrow-line region (NLR) that is roughly co-spatial with the radio jet and lobe emission (e.g., Wilson & Ulvestad 1987). The NLR has been extensively characterized by narrow-band imaging and IFU studies (Evans et al. 1991; Macchetto et al. 1994; Capetti et al. 1997; Veilleux et al. 2003). The biconical ionization cone has been observed out to radii of $\gtrsim 150''$, with an apparent opening angle of $\approx 60^\circ$ centered at $PA \approx 35^\circ$ – 45° (Unger et al. 1992; Veilleux et al. 2003). The narrow-line emitting clouds are part of a large-scale, radiatively accelerated outflow with velocities up to ≈ 3200 km s^{-1} (e.g., Cecil et al. 1990; Crenshaw & Kraemer 2000; Cecil et al. 2002). The morphology of the NLR seems to primarily trace the edges of the radio lobe, suggesting that the radio outflow has swept up and compressed the interstellar gas, giving rise to enhanced line emitting regions. The energetics of the line emission indicate that it is probably photoionization dominated (Dopita et al. 2002; Groves et al. 2004). Various studies have reported strongly non-solar abundances in the ionized gas of NGC 1068, which either require large over- or underabundances of some elements (e.g., due to shocks, supernovae pollution of Nitrogen, Phosphorus, etc, or that elements like C and Fe are predominantly locked in dust grains; Kraemer et al. 1998; Oliva et al. 2001; Martins et al. 2010), or can also be explained by multi-component photoionization models with varying densities (e.g., Kraemer & Crenshaw 2000).

As we now know, the primary AGN continuum of NGC 1068 from the optical to X-rays is completely obscured along our line of sight due to the relative orientations of the disk and obscuring torus, which has a column density $N_{\text{H}} > 10^{25}$ cm^{-2} (e.g., Matt et al. 2000). Thus the only X-ray emission that we see is scattered into our line of sight. Past observations have suggested that there are two “reflectors” which contribute to the X-ray spectrum (e.g., Matt et al. 1997; Guainazzi et al. 1999). The dominant component is from Compton scattering off the inner “wall” of the neutral obscuring torus, which gives rise to the so-called “cold” Compton reflection continuum (e.g., Lightman & White 1988). This emission is characterized by a hard X-ray spectral slope with a peak around 30 keV as well as high equivalent-width fluorescent emission lines (e.g., the dominant 6.4 keV iron line; Iwasawa et al. 1997). A second reflector arises from Compton scattering off highly ionized material associated with the ionization cone. The spectral shape of the “warm” reflector should crudely mirror the intrinsic continuum, apart from a high-energy cutoff due to Compton downscattering and potentially significant absorption edges/lines in the spectrum up to a few keV due to various elements and near ~ 7 keV due to Fe (e.g., Krolik & Kriss 1995). Radiative recombination continuum and line emission (hereafter RRC and RL, respectively) from a broad range of ions and elements can also be observed in relation to the warm reflector due to photoionization followed by recombination, radiative excitation by absorption of continuum radiation and inner shell fluorescence (Guainazzi et al. 1999; Brinkman et al. 2002; Kinkhabwala et al. 2002; Ogle et al.

²⁷ With a line-of-sight column density exceeding $N_{\text{H}} = 1.5 \times 10^{24}$ cm^{-2} and therefore optically thick to Compton scattering.

2003; Kallman et al. 2014, hereafter K14). The ionized lines imply observed outflow velocities of 400–500 km s⁻¹. Photo-ionized X-ray emission is seen to extend out along the same direction and opening angle as the radio jet/lobe and NLR (Young et al. 2001).

Past observations of NGC 1068 above 10 keV have been limited by available instrumentation, where statistics were dominated by background. Here we report on new observations of NGC 1068 between 3–79 keV from *NuSTAR*, whose focusing optics reduce background contamination to unprecedented levels and thus enable a factor of $\gtrsim 10$ statistical improvement over past observations. The *NuSTAR* data allow the best characterization of the > 10 keV spectral shape to date and therefore stand to yield new insights into the nature of Compton-thick obscuration.

This paper is organized as follows: data and reduction methods are briefly detailed in §2; X-ray spectroscopic constraints for NGC 1068 are investigated in §4, with particular attention to modeling the nucleus and galaxy host contamination; in §5 we discuss some implications of the best fit model; and finally we summarize and explore future prospects in §6. We adopt a Galactic neutral column density of $N_{\text{H}} = 3.0 \times 10^{20}$ cm⁻² (Kalberla et al. 2005) toward the direction of NGC 1068 and a redshift of 0.00379 (Huchra et al. 1999). Unless stated otherwise, errors on spectral parameters are for 90% confidence, assuming one parameter of interest.

2. OBSERVATIONAL DATA AND REDUCTION METHODS

Due to the natural limitations of various X-ray instruments in terms of energy coverage and spectral and angular resolution, our strategy was to analyze together several high-quality X-ray observations of NGC 1068 obtained by the *NuSTAR*, *Chandra*, and *XMM-Newton* observatories, collected between 2000–2013. While *NuSTAR* and *XMM-Newton* have superior collecting areas and energy coverage, neither is able to spatially separate the spectra of the AGN from various sources of host contamination or resolve some line complexes. We therefore use the *Chandra* data for these tasks, allowing us to construct the most robust model to date for the nuclear X-ray spectrum of NGC 1068. We additionally use *Swift*, *Suzaku*, and *BeppoSAX* for points of comparison. The basic parameters of these observations are listed in Table 1. All data were downloaded through the High Energy Astrophysics Science Archive Research Center BROWSE facility.

For observatories which operate multiple detectors simultaneously (e.g. EPIC *pn* and MOS aboard *XMM-Newton*), we model the data from the different detectors with all parameters tied between the spectra, incorporating a multiplicative cross-normalization constant in an attempt to account for any residual internal cross-calibration uncertainties between the instruments. Likewise, to account for external cross-calibration discrepancies between observatories, we also adopt multiplicative cross-normalization constants. The internal cross-calibration differences for instruments in the same energy range are generally known to be within $\sim 5\%$ of unity for all such missions, while cross-calibration differences both for instruments with widely different energy ranges and between instruments from different observatories can be as high as $\sim 30\%$ (see Table 1). All of the final spectra have been binned to contain a minimum of 25 counts per bin, sufficient for χ^2 minimization.

2.1. *NuSTAR*

The *NuSTAR* observatory is the first focusing satellite with sensitivity over the broad X-ray energy band from 3–79 keV (Harrison et al. 2013). It consists of two co-aligned X-ray optics/detector pairs, with corresponding focal plane modules FPMA and FPMB, which offer a 12.5×12.5 field-of-view, angular resolutions of 18'' Full Width Half Max (FWHM) and 1' Half Power Diameter (HPD) over the 3–79 keV X-ray band, and a characteristic spectral resolution of 400 eV (FWHM) at 10 keV. NGC 1068 was observed by *NuSTAR* between 2012 December 18–21.

The *NuSTAR* data were processed using the standard pipeline (NUPIPELINE; Perri et al. 2014) from the *NuSTAR* Data Analysis Software (v1.3.0) within the HEASoft package (v6.15), in combination with CALDB v20131007. The unfiltered event lists were screened to reduce internal background at high energies via standard depth corrections, as well as to remove South Atlantic Anomaly (SAA) passages. The NUPRODUCTS program was used to extract data products from the cleaned event lists for both focal plane modules FPMA and FPMB.

NGC 1068 is the only well-detected source in the *NuSTAR* FOV (see Figure 1) and appears unresolved. The campaign was spread over three observations (60002030002, 60002030004, and 60002030006) comprising 123.9 ks in FPMA and 123.7 ks in FPMB. NGC 1068 appeared as a point source for *NuSTAR* (Figure 1), and thus spectral products and lightcurves from both the nucleus and the galaxy emission (diffuse + point sources) were extracted using 75'' radius apertures (corresponding to $\approx 81\%$ encircled energy fraction), with backgrounds estimated from blank regions free of contaminating point sources on the same detector (see Figure 1). We find that NGC 1068 is securely detected up to ≈ 55 keV at 3σ confidence with *NuSTAR*, and has a maximum signal-to-noise of ≈ 26 around the peak of Fe K α .

We also generated a model of the expected background for each FPM within our adopted aperture using NUSKYBGD (Wik et al. 2014). NUSKYBGD uses several user-defined background regions to sample all four detectors in each FPM, which it simultaneously fits in order to model the spectral and angular dependencies for several background components (e.g., instrumental, focused, and unfocused), before ultimately generating the expected background within the adopted aperture. We confirmed the similarity, particularly at high energies where the background makes a significant contribution, between the local and model backgrounds to a few percent. Ultimately we adopted the local background for simplicity.

Custom position-dependent response matrices and ancillary response files were generated for the spectra of each module, which provide nominal vignetting and PSF aperture corrections. In total, we have $\approx 27,300$ and $\approx 26,100$ counts between 3–79 keV in FPMA and FPMB, respectively. As can be seen in Figure 2, the FPMA and FPMB spectra are in excellent agreement, and thus we merged them into a single spectrum using exposure-weighting for convenience and we use this spectrum for all fitting and plotting purposes (from Figure 3 on). With respect to the *XMM-Newton* EPIC *pn* instrument, preliminary results suggest *NuSTAR* normalization offsets of 1.11 ± 0.01 ; this value is fully consistent with other *NuSTAR/XMM-Newton* cross-calibration studies (e.g., Walton et al. 2013, 2014). Due to the high signal-to-noise of the *NuSTAR* data, we also find that we need to apply a $\approx +40$ eV energy offset (i.e., ≈ 1 spectral bin) to bring the intrinsic Fe K α line energy (6.4007 keV) into agreement with

TABLE 1
 X-RAY OBSERVATIONS

Instrument	Date	Obsid	Exp.	Energy Band	Aperture	Count Rate	Norm Offset
<i>BeppoSAX</i> MECS	1996-12-30	5004700100	100.8	3–10	180	0.06	1.13±0.02
<i>BeppoSAX</i> PDS	1996-12-30	5004700100	116.6	15–140	...	0.27	0.70±0.10*
<i>BeppoSAX</i> MECS	1998-01-11	5004700120	37.3	3–10	180	0.04	1.11±0.02
<i>BeppoSAX</i> PDS	1998-01-11	5004700120	31.5	15–140	...	0.28	0.70±0.10*
<i>Chandra</i> ACIS-S	2000-02-21	344	47.7	0.4–8	2–75	2.09	1.04±0.04
<i>XMM-Newton</i> pn	2000-07-29	0111200101	32.8	0.2–10	75	12.36	1.00
<i>XMM-Newton</i> pn	2000-07-30	0111200201	28.7	0.2–10	75	12.36	1.00
<i>Chandra</i> HETG HEG/MEG	2000-12-04	332	25.7	0.3–8	2	0.031/0.085	1.09±0.06, 1.05±0.06
<i>Suzaku</i> XIS	2007-02-10	701039010	61.5	0.3–9	260	0.73	1.17±0.02
<i>Suzaku</i> HXD PIN	2007-02-10	701039010	38.8	15–70	...	0.40	1.20±0.05*
<i>Chandra</i> HETG HEG/MEG	2008-11-18	10816	16.2	0.8–10/0.4–8	2	0.029/0.078	1.09±0.06, 1.05±0.06
<i>Chandra</i> HETG HEG/MEG	2008-11-19	9149	89.4	0.8–10/0.4–8	2	0.027/0.077	1.09±0.06, 1.05±0.06
<i>Chandra</i> HETG HEG/MEG	2008-11-20	10815	19.1	0.8–10/0.4–8	2	0.028/0.076	1.09±0.06, 1.05±0.06
<i>Chandra</i> HETG HEG/MEG	2008-11-22	10817	33.2	0.8–10/0.4–8	2	0.028/0.079	1.09±0.06, 1.05±0.06
<i>Chandra</i> HETG HEG/MEG	2008-11-25	10823	34.5	0.8–10/0.4–8	2	0.029/0.077	1.09±0.06, 1.05±0.06
<i>Chandra</i> HETG HEG/MEG	2008-11-27	9150	41.1	0.8–10/0.4–8	2	0.028/0.077	1.09±0.06, 1.05±0.06
<i>Chandra</i> HETG HEG/MEG	2008-11-30	10829	39.6	0.8–10/0.4–8	2	0.027/0.079	1.09±0.06, 1.05±0.06
<i>Chandra</i> HETG HEG/MEG	2008-12-03	10830	44.0	0.8–10/0.4–8	2	0.029/0.078	1.09±0.06, 1.05±0.06
<i>Chandra</i> HETG HEG/MEG	2008-12-05	9148	80.2	0.8–10/0.4–8	2	0.029/0.078	1.09±0.06, 1.05±0.06
<i>Swift</i> BAT (70-month)	2004–2010	...	9250.0	14–195	...	4.97×10^{-5}	0.75±0.10*
<i>NuSTAR</i> FPMA/FPMB	2012-12-18	60002030002	56.9/56.8	3–79	75	0.22/0.21	1.11±0.01
<i>Swift</i> XRT	2012-12-19	00080252001	2.0	0.5–10	75	0.44	1.13±0.25
<i>NuSTAR</i> FPMA/FPMB	2012-12-20	60002030004	47.8/47.5	3–79	75	0.22/0.21	1.11±0.01
<i>NuSTAR</i> FPMA/FPMB	2012-12-21	60002030006	19.2/19.4	3–79	75	0.22/0.21	1.11±0.01

NOTE. — *Column 1*: Satellite and instrument. *Column 2*: Starting date of observation. *Column 3*: Observation identification (obsid) number. *Chandra* frametimes were ≈ 1.9 – 2.1 s, except for obsids 355, 356, and 2454 with 3.2 s and obsids 365, 9140, and 10937 with 0.3–0.4 s. *Column 4*: Exposure time in ksec. *Column 5*: Energy band in keV. *Column 6*: Extraction aperture radius in arcseconds. If a range is given, then an annular region was extracted. For the HETG, the values given represent the half-width of the extraction region in the cross-dispersion direction. *Column 7*: Count rate in counts s^{-1} . *Column 8*: Relative normalization offset with respect to the pn in the 3–7 keV band. However, entries denoted by *s are in fact relative to combined *NuSTAR* FPMA/FPMB spectrum in the 20–60 keV band.

the established redshift of NGC 1068 and the high significance line energy determined by the *Chandra* High Energy Transmission Grating (HETG Canizares et al. 2000); the reason for the offset is not known, however, its value is within the nominal calibration precision of *NuSTAR* and somewhat smaller offsets have been observed in other sources.

2.2. *XMM-Newton*

NGC 1068 was observed on 2000 July 29–30 with *XMM-Newton* using the EPIC pn and MOS1/MOS2 instruments (Jansen et al. 2001), which provide respective angular resolutions of ≈ 5 – $6''$ FWHM and 14–15'' HPD over the 0.15–12 keV X-ray band, respectively. Although the energy resolution of the EPIC detectors (FWHM ≈ 45 –150 eV between 0.4–8 keV) is poorer than the HETG, the difference narrows to a factor of only ≈ 5 by 6–8 keV, and the three EPIC detectors have substantially larger effective areas compared to *Chandra*. This improvement in counting statistics allows us to obtain novel constraints on the nuclear spectrum of NGC 1068 compared to the HETG spectra alone.

The *XMM-Newton* observation of NGC 1068 was split into two segments made using the Medium filter in Large Window mode (48 ms frame-time) for the pn, in Full Frame mode (1.4 s frame-time) for MOS1, and in Small Window mode (0.3 s frame-time, $110'' \times 110''$ FOV) for MOS2. Given the X-ray flux from the AGN, these options mean that MOS1 will be slightly piled-up while MOS2 will not sample the entire 75'' radius extraction region (missing some extended emission and requiring a larger PSF correction). To limit systematic uncertainties, we opted to only extract counts for the pn instrument, which comprises 60% of the total *XMM-Newton* collecting area (i.e., MOS1+MOS2+pn). These are effectively the same conclusions arrived at by Matt et al. (2004, hereafter M04).

We processed both data sets using SAS (v13.0.0) and selected only single and double events with quality flag=0. The events files were filtered to exclude background flares selected from time ranges where the 10–12 keV count rates in the pn camera exceeded 0.3 c/s. The remaining good exposures are 32.8 ks for the first observation and 28.7 ks for the second observation, with $\approx 760,000$ counts between 0.2–10.0 keV.

Source spectra were extracted from a circular region of 75'' radius (corresponding to an $\approx 93.5\%$ encircled energy fraction) centered on the nucleus, to match the *NuSTAR* extraction region. Background photons were selected from a source-free region of equal area on the same chip as the source. We constructed response matrices and ancillary response files using the tasks RMFGEN and ARGEN for each observation. Given that the two observations are consecutive and constant within their errors, we merged the spectral products using exposure-weighting. As mentioned previously, we base all of the normalization offsets relative to the *XMM-Newton* pn, which thus has a value of 1.00. Additionally, we find we need to apply a $\approx +15$ eV energy offset (i.e., ≈ 1 response bin) to bring the intrinsic Fe $K\alpha$ line energy (6.4007 keV) into agreement with the established redshift of NGC 1068 and the high significance line energy determined by the *Chandra* HETG.

2.3. *Chandra* HETG and ACIS-S

NGC 1068 was observed on multiple occasions with *Chandra* with both the ACIS-S detector (Garmire et al. 2003) by itself and the HETG placed in front of the ACIS-S. By itself, ACIS-S has a angular resolution of $< 0.5''$ FWHM and $\lesssim 0.7''$ HPD, and a spectral resolution of FWHM ≈ 110 –180 eV between 0.4–8 keV. The HETG consists of two different grating assemblies, the High Energy Grating (HEG) and the Medium Energy Grating (MEG), which provide rela-

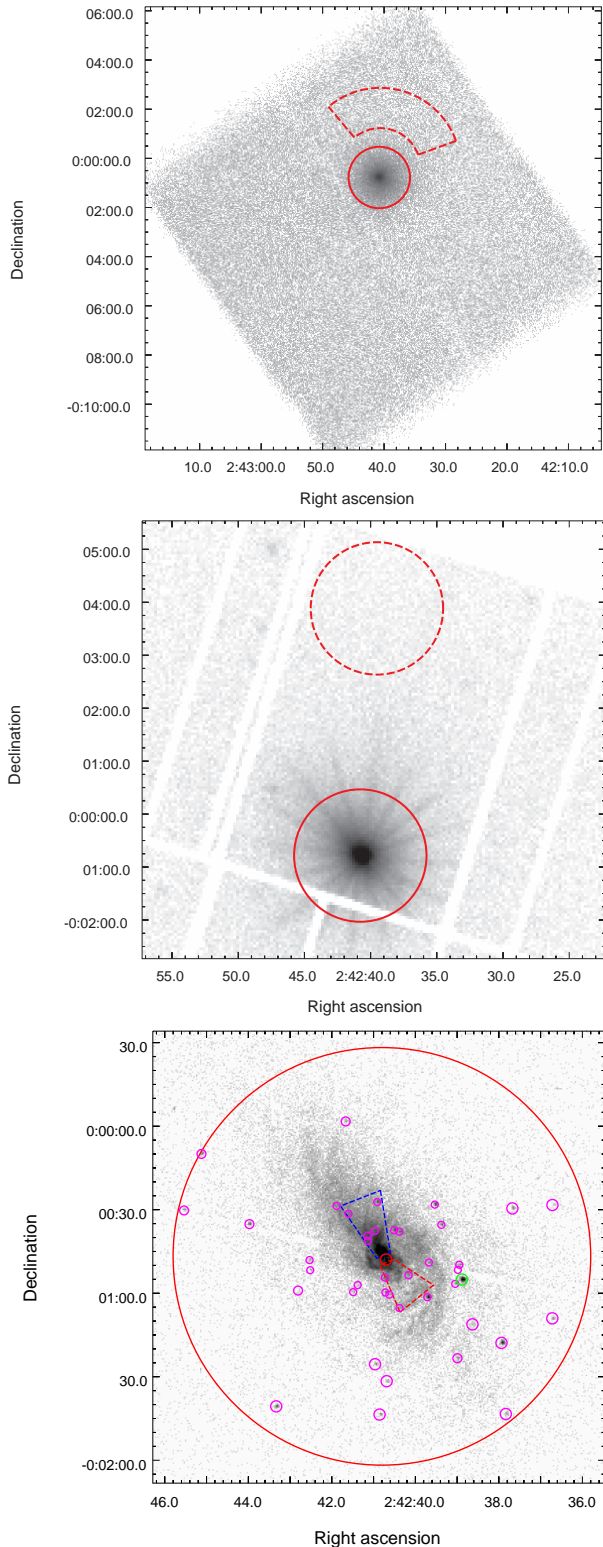


FIG. 1.— (top) *NuSTAR* 3–79 keV FPMA image of NGC 1068 showing the $75''$ radius source (solid red circle) and polygon background (dashed red circle) extraction regions. (middle) *XMM-Newton* 0.2–10 keV pn image of NGC 1068 showing the $75''$ radius source (solid red circle) and polygon background (dashed red circle) extraction regions. The central point source dominates, although there are hints of faint extended emission. (bottom) *Chandra* 0.5–8.0 keV ACIS-S image of NGC 1068 showing the $75''$ radius aperture used for *NuSTAR* and *XMM-Newton* (large solid red circle). The nucleus is denoted by the small $2''$ radius (solid red) aperture and is strongly piled up. The obvious off-nuclear point sources (denoted by 2 – $3''$ radius magenta circles) and diffuse emission between 2 – $75''$ were extracted separately. The rough positions of the radio jet (blue dashed region) and counter jet (red dashed region) are shown (Wilson & Ulvestad 1987). The brightest off-nuclear point source in the *Chandra* image (green circle) is not present after 2000-12-04 and thus has been excluded from analysis. A background was extracted from a source free region on the same chip, outside this figure.

tively high spectral resolution (HEG: 0.0007–0.154 eV; MEG: 0.0004–0.063 eV) over the entire *Chandra* bandpass (HEG: 0.8–10 keV; MEG: 0.4–8 keV). The gratings operate simultaneously, with the MEG/HEG dispersing a fraction of the incident photons from the two outer/inner High Resolution Mirror Assembly (HRMA) shells, respectively, along dispersion axes offset by 10° , such that they form a narrow X-shaped pattern on the ACIS-S detector. Roughly half of the photons that are not absorbed by the grating pass through undispersed (preferentially the higher-energy photons) and comprise the HETG 0th order image on ACIS-S with the standard spectral resolution.

All of the *Chandra* data were reduced following standard procedures using the CIAO (v4.5) software package and associated calibration files (CALDB v4.5.5.1). The data were reprocessed to apply updated calibration modifications, remove pixel randomization, apply the energy-dependent sub-pixel event-repositioning (EDSER) techniques, and correct for charge transfer inefficiency (CTI). The data were filtered for standard *ASCA* grade selection, exclusion of bad columns and pixels, and intervals of excessively high background (none were found). Analysis was performed on reprocessed *Chandra* data, primarily using CIAO, but also with custom software.

The 1st-order HETG spectral products were extracted using standard CIAO tools using a HEG/MEG mask with a full-width of $4''$ in the cross-dispersion direction centered on the NGC 1068 nucleus; anything smaller than this will suffer from significant energy-dependent PSF losses. The intrinsic ACIS-S energy resolution allows to separate the overlapping orders of the dispersed spectra. The plus and minus sides were combined to yield single HEG and MEG 1st-order spectra. All of the HETG data were combined after double-checking that they did not vary to within errors; obsID 332 appears to have a modestly higher count rate, but this difference is largely below 2 keV and does not materially affect the combined >2 keV spectra. In total, we have 438.7 ks of HETG-resolution nuclear spectra available for spectral fitting (see Table 1 for details), with $\approx 12,500$ HEG counts between 0.8–10.0 keV and $\approx 34,000$ MEG counts between 0.4–8.0 keV. We consider these to be the least contaminated AGN spectra available below 10 keV (hereafter, simply the HETG “AGN” spectra). The normalization offset between the HEG and MEG was found to be 1.03 ± 0.07 , while the offsets with respect to the pn were 1.05 ± 0.06 and 1.09 ± 0.06 , respectively. This is consistent with the cross-calibration finding in Marshall (2012) and Tsujimoto et al. (2011).

In principle, we have a similar amount of HETG 0th-order data, in addition to 47.7 ks of normal ACIS-S data that could be used to model the extranuclear contamination which strongly affects the lower-energy *NuSTAR* and *XMM-Newton* spectra. However the calibration of the HETG 0th-order still remains somewhat uncertain above ~ 5 keV (M. Nowak, private communication), which we consider critical for extrapolating into the *NuSTAR* band. Thus we chose to model the contamination spectra solely using ACIS-S obsid 344. These data were taken with the nominal 3.2s frame time, such that the nucleus is heavily piled-up ($\sim 40\%$) within 1 – $2''$. We therefore excluded the inner $2''$ from the contamination analysis and consider the 2 – $75''$ ACIS-S spectrum to be predominantly emission from the host galaxy (hereafter “host”), although we must consider contributions from the broad wings of the PSF (which only contribute ≈ 5 – 10% beyond $2''$ based on PSF simulations) and any truly extended Compton reflec-

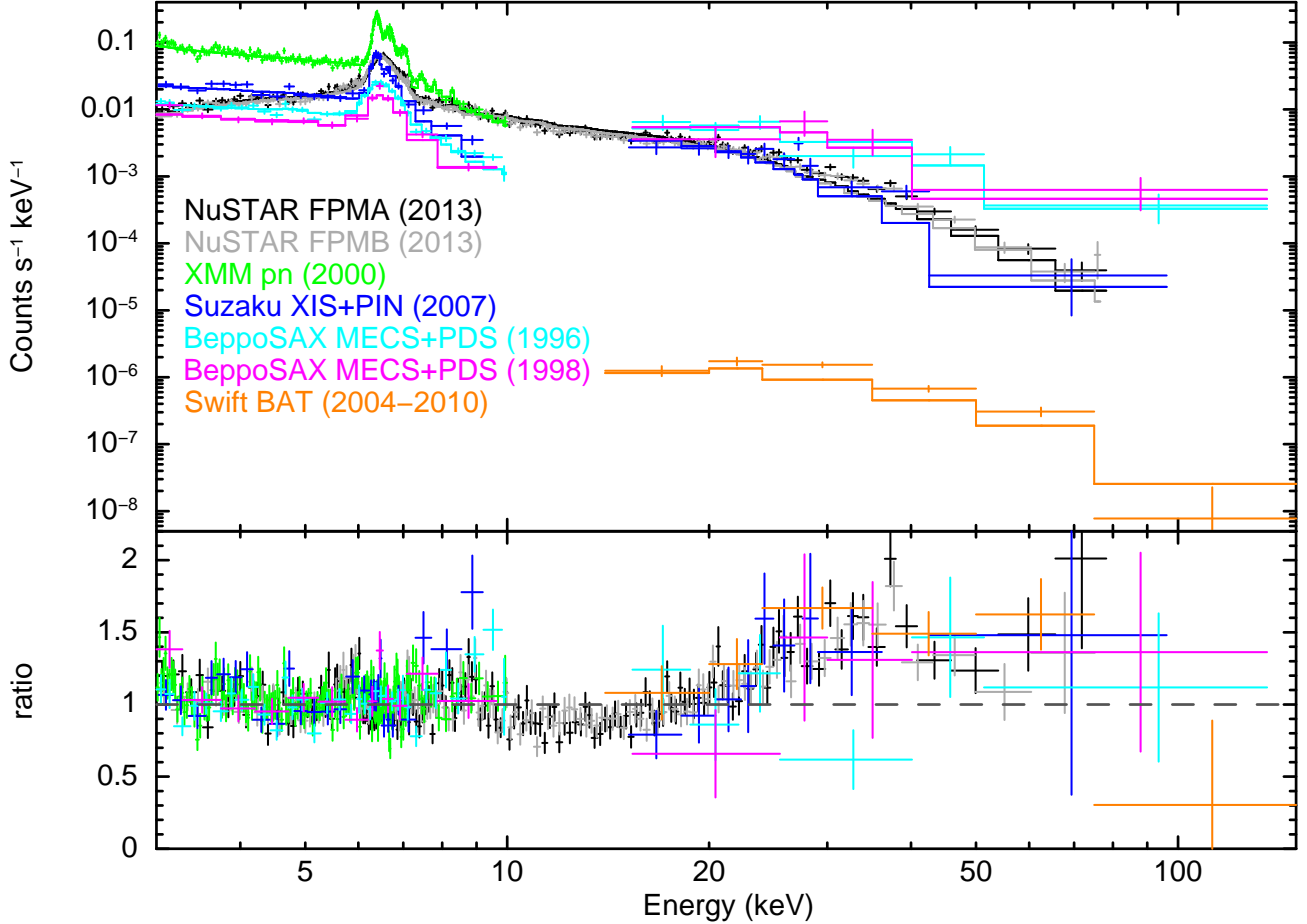


FIG. 2.— Comparison of the *NuSTAR* FPMA/FPMB (black/grey) and *XMM-Newton* pn (green) spectra with other past observations of NGC 1068 from *Suzaku* XIS+PIN (blue), *BeppoSAX* MECS+PDS 1996 (magenta), *BeppoSAX* MECS+PDS 1998 (cyan), and *Swift* BAT (orange), all modeled with the best-fitted two-reflector model M04a. The top panel shows the observed spectra while the bottom panel shows the data-to-model ratios for each spectrum. There is good overall consistency between the various datasets once known normalization offsets are accounted for, with only a few marginally discrepant points seen from the 1996 *BeppoSAX* data. It is clear from the bottom panel that the model provides a poor fit to the data near the Compton reflection hump, with the data peaking at ~ 30 keV while the `pexrav` model peaks at ~ 20 keV. There are some additional residuals around 10–15 keV indicating the curvature of the reflection is more severe than the model predicts, as well as around the Fe/Ni line region (≈ 6 –8 keV), suggesting that a few Gaussian lines are insufficient for modeling the complex Fe/Ni emission.

tion and scattered components from the intrinsic nuclear emission (hereafter “extended AGN”). We replaced readout streak events from the nucleus with an estimate of the background using the `ACISREADCORR` tool.

We note that the brightest off-nuclear point source, CXOU J024238.9–000055.15, which lies $30''$ to the southwest of the nucleus in the 344 observation, provides $\sim 20\%$ of the host contamination counts above 4 keV. Notably, it is not present after 2000-12-04 in either the *Chandra* or *Swift* observations, the latter of which is simultaneous with the *NuSTAR* observation (see §2.6). Thus we excluded this point source from our assessment of the host contamination contribution to the *NuSTAR* spectra. The source is present and distinct during the *XMM-Newton* observations, and is found to comprise $\approx 1.5\%$ of the > 4 keV counts (see also the extended discussion in M04). For simplicity, we account for its presence in the *XMM-Newton* spectrum of NGC 1068 using an additional normalization adjustment between *XMM-Newton* and *NuSTAR*.

To assess host contamination, initially we extracted ACIS-S spectra of obvious point sources and diffuse emission separately, as shown in Figure 1, using `SPECSEXTRACT`. For

the point sources, we used 2 – $3''$ extraction radii, depending on whether they are strong or weak and whether they reside within strong diffuse emission, while for the diffuse emission we extracted everything else between 2 – $75''$. In total, we found ≈ 6300 and ≈ 93450 0.4–8.0 keV counts for the off-nuclear point source and diffuse components, respectively. A local background region was extracted from an adjacent region $100''$ in radius ≈ 3.5 northwest of NGC 1068. Ultimately, to simplify the contamination model and improve statistics, we also extracted a total contamination spectrum of all emission within 2 – $75''$. The normalization offset between the pn and ACIS-S was 1.04 ± 0.04 , which is consistent with the values found by Nevalainen et al. (2010) and Tsujimoto et al. (2011).

2.4. *BeppoSAX*

NGC 1068 was observed by *BeppoSAX* on 1996 December 30 and on 1998 January 11 with the Low Energy Concentrator Spectrometer (LECS), the three Medium Energy Concentrator Spectrometers (MECS), and Phoswich Detector System (PDS). We use only the MECS and PDS here.

The MECS contains three identical gas scintillation propor-

tional counters, with an angular resolution of ≈ 0.7 FWHM and ≈ 2.5 HPD, and a spectral resolution of $\text{FWHM} \approx 200\text{--}600$ eV between 1.3–10 keV. MECS1 failed a few months after launch and thus only MECS2 and MECS3 data are available for the 1998 observation. The MECS event files were screened adopting standard pipeline selection parameters. Spectra were extracted from $3'$ radii apertures and the spectra from individual units were combined after renormalizing to the MECS1 energy-PI relation. Background spectra were obtained using appropriate blank-sky files from the same region as the source extraction. The resulting MECS spectra have ≈ 5900 counts between 3–10 keV in 100.8 ks of good exposure for the first observation and ≈ 1550 counts in 37.3 ks for the second observation. We find that the MECS normalization is systematically offset from the pn by a factor of 1.12 ± 0.02 in the 3–7 keV band and thus by a factor of 1.02 ± 0.02 with respect to *NuSTAR* in the same band.

The PDS has no imaging capability, but does have sensitivity between 15–220 keV and can potentially provide some constraints above the *NuSTAR* band. The PDS data were calibrated and cleaned using the SAXDAS software within HEASoft, adopting the ‘fixed Rise Time threshold’ method for background rejection. The PDS lightcurves are known to show spikes on timescales of fractions of second to a few seconds, with most counts from the spikes typically falling below 30 keV. We screened the PDS data for these spikes following the method suggested in the NFI user guide,²⁸ arriving at $\approx 16,600 \pm 3010$ counts between 15–220 keV in 62.5 ks of good exposure for the first observation and $\approx 4720 \pm 1560$ counts in 17.7 ks for the second observation. The PDS spectra were logarithmically rebinned between 15–220 keV into 18 channels, although we cut the spectrum at 140 keV due to poor statistics. With the data quality/binning, it is difficult to appreciate the presence of a bump at 30 keV. The PDS normalization is known to be low by $\approx 20\text{--}30\%$ (Grandi et al. 1997; Matt et al. 1997) compared to the MECS, which we accounted for by using a fixed normalization constant of 0.7 ± 0.1 when modeling the data with respect to *NuSTAR*.

We note that the statistics for the second *BeppoSAX* observation are poorer, with many of the channels statistically consistent with zero.

2.5. *Suzaku*

The *Suzaku* observatory observed NGC 1068 with the X-ray Imaging Spectrometer (XIS) and Hard X-ray Detector (HXD) PIN instruments on 2007 February 10. Our reduction follows the recommendations of the *Suzaku* Data Reduction Guide.²⁹

For the XIS, we generated cleaned event files for each operational detector (XIS0, XIS1, and XIS3) and both editing modes (3x3 and 5x5) using the *Suzaku* AEPipeline with the latest calibration, as well as the associated screening criteria files in HEASoft. Using XSELECT, source spectra were extracted using a $260''$ radius aperture, while background spectra were extracted from remaining regions free of any obvious contaminating point sources. Responses were generated for each detector using the XISRESP script with a medium resolution. The spectra for the front-illuminated detectors XIS0 and XIS3 were consistent, and were subsequently combined using ADDASCASPEC; for simplicity, we adopt this composite spectrum to represent the XIS. We obtained $\approx 33,300$ counts with a good exposure of 61.5 ks. We find that the XIS spectrum

is systematically offset from the pn by a factor of 1.17 ± 0.02 , which is slightly (i.e., $< 3\sigma$) above the expected normalization offset of 1.10 ± 0.01 assessed by Tsujimoto et al. (2011).

Similar to the PDS, the PIN has poor angular resolution ($0.56^\circ \times 0.56^\circ$ FOV) but does have sensitivity between 15–70 keV and thus provides another point of comparison with *NuSTAR*. We reprocessed the unfiltered event files following the data reduction guide to obtain $\approx 15,500$ counts with a good exposure of 39.0 ks. No significant detection was found in the GSO. Since the HXD is a collimating instrument, estimating the background requires separate consideration of the non X-ray instrumental background (NXB) and cosmic X-ray background (CXB), which comprise $\approx 89\%$ of the total counts. We used the response and NXB files provided by the *Suzaku* team,³⁰ adopting the model D ‘tuned’ background. Spectral products were generated using the HXD PINXBPI tool, which extracts a composite background using the aforementioned NXB and a simulated contribution from the expected CXB following Boldt (1987). We find the PIN normalization to be systematically offset from *NuSTAR* by a factor of 1.2 ± 0.05 , which is consistent with the current cross-calibration uncertainty (K. Madsen et al., submitted).

2.6. *Swift*

The *Swift* observatory observed NGC 1068 with the X-ray Telescope (XRT; $7''$ FWHM, $20''$ HPD) for ≈ 2 ks simultaneous with *NuSTAR* on 2012 December 19. The processed data were retrieved from the *Swift* archive, and analysis was performed using FTOOLS. With ≈ 1200 counts between 0.5–10 keV in a $75''$ aperture, the *Swift* exposure is not long enough to provide additional constraints beyond those already obtained with *NuSTAR*, *XMM-Newton*, and *Chandra*. However, it does serve to determine if any transient point sources strongly contributed to the < 10 keV *NuSTAR* spectra of NGC 1068. To this end, we generated a 0.5–10 keV image with XSELECT, which is consistent with the *Chandra* images from 2008 to within the limits of the *Swift* XRT angular resolution and does not show any new strong off-nuclear point sources. We find the XRT 3–10 keV composite spectrum is consistent with the other instruments aside from its normalization, which is systematically offset from the pn by a factor of 1.12 ± 0.25 ; the large error bar is due to the fact that the observation only has 64 counts in the 3–10 keV band. This offset is fully consistent with those found by Tsujimoto et al. (2011).

Since November 2004, the Burst Alert Telescope (BAT) onboard *Swift* (Gehrels et al. 2004) has been monitoring the hard X-ray sky (14–195 keV) and can potentially provide some constraints above the *NuSTAR* band. *Swift* BAT uses a 5200 cm^2 coded-aperture mask above an array of 32,768 CdZnTe detectors to produce a wide field of view of 1.4 steradian of the sky and an effective resolution of $\approx 20'$ (FWHM) in stacked mosaicked maps. Based on the lack of variability (see §3), we used the stacked 70-month spectrum, which is extracted from the central pixel ($2.7'$; Baumgartner et al. 2013) associated with the BAT counterpart, to assess nature of the emission. The background-subtracted spectrum contains ≈ 460 counts in the 14–195 keV band. We find the BAT normalization to be systematically offset from *NuSTAR* by a factor of 0.75 ± 0.05 , which is consistent with the current cross-calibration uncertainty (K. Madsen et al., in preparation).

²⁸ <http://heasarc.nasa.gov/docs/sax/abc/saxabc/saxabc.html>

²⁹ <http://heasarc.gsfc.nasa.gov/docs/suzaku/analysis/>

³⁰ <http://www.astro.isas.ac.jp/suzaku/analysis/hxd/>

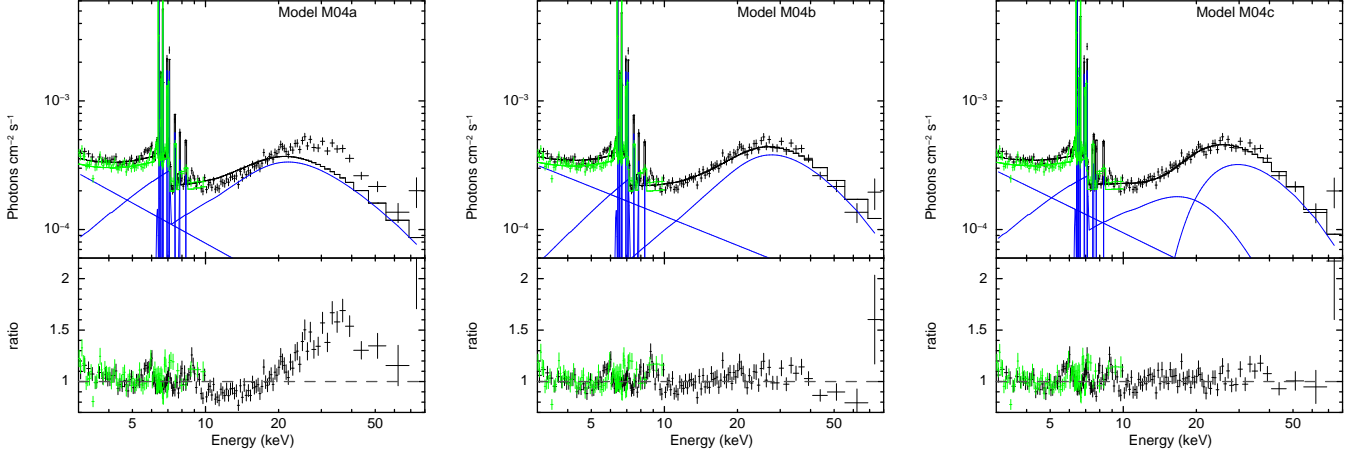


FIG. 3.— Comparison of the *NuSTAR* (black) and *XMM-Newton* pn (green) spectra of NGC 1068, modeled with the best-fitted two-reflector model (blue) where several variables are fixed (*left*; model M04a), fit as free parameters (*middle*; model M04b), and with the addition of a leaky, absorbed transmission component (*right*; model M04c). The top panel shows the observed spectra while the bottom panel shows the data-to-model ratios for each spectrum. The overall fits with the parameters free and the addition of the transmission component (e.g., George et al. 2000) are better, with most of the residuals confined to the complex Fe/Ni line region.

3. X-RAY VARIABILITY CONSTRAINTS

Depending on the location and structure of the obscuration in NGC 1068, it may be possible to observe temporal variations in one or more of its spectral components on short or long timescales. Notably, there have been previous claims of low-significance variability from the warm reflection component between the *BeppoSAX* and *XMM-Newton* observations (Guainazzi et al. 2000; Matt et al. 2004).

As shown in Table 1, we find reasonable consistency between the count rates extracted from all instruments where NGC 1068 was observed more than once, with differences always less than 3σ based on counting statistics. These constraints imply there is no strong continuum variability below 10 keV over periods of 10–15 years. Since *Swift* BAT continuously observes the sky, a new snapshot image can be produced every ~ 1 week for persistent high-energy X-ray sources due to the wide field of view and large sky coverage. To study long-term variability of NGC 1068 (SWIFT_J0242.6+0000) above 10 keV, we use the publicly available 70-month (9.3 Ms) lightcurves from *Swift* BAT (Baumgartner et al. 2013), which span 2004–2010. The wide energy range of *Swift* BAT allows us to test any underlying energy dependence of the lightcurve, assessing lightcurves in eight non-overlapping energy bands: 14–20, 20–24, 24–35, 35–50, 50–75, 75–100, 100–150, 150–195 keV. The cumulative 14–195 keV lightcurve, binned in half-year intervals due to the limited statistics, is shown in Figure 4 and is formally constant to within errors ($\chi^2_\nu = 0.95$ for $\nu = 17$ degrees of freedom). Variability limits in the individual bands are consistent with the full band results, but generally are less constraining due to limited statistics.

To investigate short-term variability, we applied the Kolmogorov-Smirnov (K-S) test to individual observations, finding all observations to be constant in count rate with 3σ confidence. We searched for additional hints of short-term variability taking advantage of the high throughput of *NuSTAR* above 10 keV. The timescales covered by these light curves (~ 1 –200 ks) can only reveal rapid fluctuations, such as those expected from the intrinsic powerlaw emission. Therefore, any variability seen in this range would be indicative of a transmitted powerlaw component (e.g. Markowitz et al. 2003;

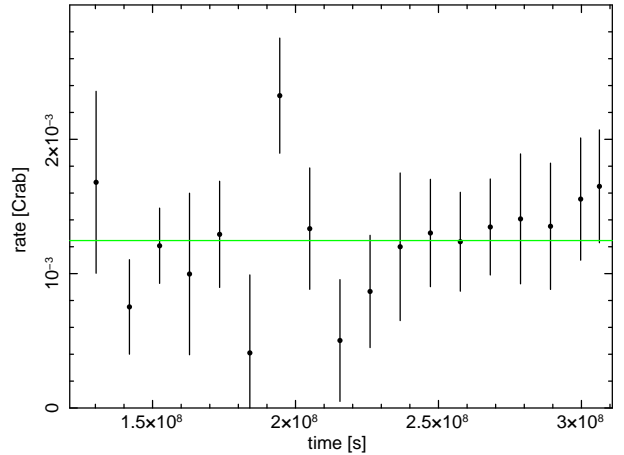


FIG. 4.— *Swift* BAT 70-month 14–195 keV light curve spanning 2004–2010, in bins of ≈ 0.5 yr. The green line denotes the best-fitted constant model ($\chi^2_\nu = 0.95$ for $\nu = 17$), indicating that NGC 1068 shows no significant hard X-ray variability over this time span.

McHardy et al. 2004, 2005, 2006; Markowitz et al. 2007). In Figure 5, we constructed power spectra from the high-energy *NuSTAR* lightcurves for NGC 1068 and a typical background region, which we compare to the expected power spectra for pure Poisson noise and for the expected variability of a pure transmitted component, as observed in unobscured AGN of similar mass and accretion rates. To produce this, we extracted 30–79 keV counts from our nominal source region and a background region of equal area on the same detector using XSELECT. We constructed lightcurves in 100 s equally spaced bins, retaining only those which had exposure ratios over 90%. Note that the nature of *NuSTAR*'s orbit means that for the given sky location we will have 2 ks gaps in the lightcurves every 6 ks. Moreover, since *NuSTAR* observed NGC 1068 in three distinct segments, we have larger gaps in between the observations. To mitigate these potential sources of aliasing, we calculated power spectra using the Mexican-hat filtering method described in Arévalo et al. (2012), which is largely unaffected by gaps in the lightcurves. Finally, we normalized the power as the variance divided by the square

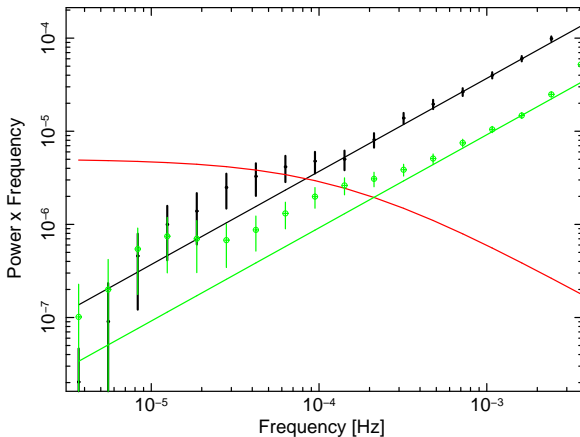


FIG. 5.— Power spectra of the combined 30–79 keV band lightcurves from *NuSTAR* for NGC 1068. The source and background power spectra are plotted in black and green symbols, respectively. The black and green lines denote the power spectra expected for Poisson noise only for each case. The solid red curve represents the power spectrum of the direct continuum for an AGN of the same mass and accretion rate as NGC 1068. The high-energy lightcurves are roughly consistent (at $\approx 2\sigma$) with simple Poisson noise, although there could be additional low-frequency noise that affects both the source and background variability. Furthermore, backgrounds extracted from the other *NuSTAR* FPM detectors produced similar shapes. Thus we conclude that the variability constraints are significantly below the expected value for a transmitted AGN continuum.

of the average count rate. As can be seen in Figure 5, the power spectrum detected from NGC 1068 is fully consistent with Poisson noise at better than 2σ .³¹ Thus, if there is any transmitted component leaking through, it does not comprise the bulk of the > 10 keV flux.

We conclude that if there has been any variability from NGC 1068 in the past ≈ 15 years, it has been at a level comparable to either the cross-calibration uncertainties between instruments or the statistical uncertainty in the data and that the short-term behaviour as measured by the *NuSTAR* lightcurves is not consistent with a transmitted powerlaw component dominating the flux above 10 keV.

4. X-RAY SPECTRAL CONSTRAINTS

We begin by comparing the high-quality combined *NuSTAR* and *XMM-Newton* spectra to those from several past satellites to demonstrate the dramatic improvement in data quality. We compare all of these to a few common previously used models, which can eventually fit the data relatively well when pushed to extreme values. Following this, we develop a more realistic approach to quantify the non-negligible contamination from extranuclear emission and then model the AGN components using a few common models such as `pexmon` (Nandra et al. 2007), `MYTORUS` (Murphy & Yaqoob 2009; Yaqoob 2012), and `TORUS` (Brightman & Nandra 2011).

Unless stated otherwise, modeling was performed with `XSPEC v12.9.0` (Arnaud 1996), and quoted uncertainties on spectral parameters are 90% confidence limits for a single parameter of interest, and spectral fitting is performed through χ^2 minimization. Neutral absorption is treated with the `tbabs` absorption code (Wilms et al. 2000), with appropriate solar abundances (`wilm`) and cross sections (`vern`; Verner et al. 1996).

³¹ It is important to stress here that the convolution kernel is broad in frequency, such that nearby power density spectral points will be correlated. Thus the fact that several consecutive points are above the PN level does not make the detection of variability more significant.

Throughout our analysis, we assume there is no angular dependence of the nuclear emission spectral shape (such that all scatterers see the same photon index) and we neglect any accretion disk reflection component (e.g., Ross & Fabian 2005; Dauser et al. 2013; García et al. 2014) when modeling the obscured nuclear radiation, which is justified due to the inclination and dominance of scattering and absorption from distant material.

Finally, we note that `XSPEC` has considerable difficulty arriving at the best-fit solution when dealing with large numbers of free parameters, such as we have in NGC 1068 associated with the considerable line emission. Thus, to mitigate this in cases in which we fit individual emission lines separately, we individually fitted the line centers, redshifts, widths, and heights of the Gaussian lines over small portions of the spectrum above a local powerlaw continuum, and then froze each line at its best-fit values. We then fit the relative contributions from the continuum and fluorescent line models.

4.1. Comparison to Previous Models

As mentioned in §1, NGC 1068 has been successfully modeled in the past above ≈ 3 –4 keV with a double reflector comprised of both neutral “cold” (`pexrav` with $R = -1$; Magdziarz & Zdziarski 1995) and ionized “warm” (`cutoffpl`) Compton-scattered components, plus a few Gaussian emission lines to model the strong Fe and Ni emission (Matt et al. 1997; Guainazzi et al. 2000, hereafter model “M04a”, since it was adopted from M04; see also similar models from). We therefore began by fitting this model (see Table 2) to the *NuSTAR*, *XMM-Newton*, *BeppoSAX*, *Suzaku*, and *Swift* BAT spectra above 3 keV.

We initially fixed most of the parameters to the values found by M04³² (e.g., $\Gamma = 2.04$, $Z_{\text{Fe}} = 2.4Z_{\odot, \text{Fe}}$, $\theta_{\text{inc}} = 63^\circ$, $E_{\text{cut}} = 500$ keV), varying only the component normalizations and the redshifts of the emission lines. The normalizations were coupled between the different instruments while the redshifts differed for each instrument to account for the aforementioned linear energy offsets. The redshifts of the cold reflector and neutral lines ($K\alpha$, $K\beta$) were tied and allowed to vary as one parameter, while the redshifts of the ionized lines were tied and allowed to vary as another parameter. The best fit of this dual-reflector model, M04a, yielded a reduced $\chi^2_\nu = 1.40$ for $\nu = 1785$. As can be seen in Figure 2, the fit has strong residuals near the Compton reflection hump due to a discrepancy between the peak of the reflection hump in the data (~ 30 keV) and the one from the `pexrav` model (~ 20 keV). We also see residuals around 10–15 keV, implying that there is stronger curvature in the actual reflection spectrum than has been modeled, as well as around the Fe/Ni line complex, suggesting that the Gaussians are not sufficient to describe the line complexity observed.

The bottom panel of Figure 2 shows the data-to-model ratios for several past hard X-ray missions compared against the best-fitted fixed- Γ two-reflector model. As noted in §3, there have been previous claims of low-level variability in the warm reflection component (Guainazzi et al. 2000; Matt et al. 2004). After accounting for known cross-calibration offsets, we find that the *NuSTAR*, *XMM-Newton* pn, *Suzaku* XIS, and *BeppoSAX* MECS spectra in the 3–5 keV range, where the warm reflector should dominate, are consistent within their statistical uncertainties based on powerlaw fits to this

³² Note that in `pexrav`, the inclination angle is specified in units of $\cos 90 - \theta_{\text{inc}}$, such that a value of 0.88 is equivalent to 63° .

TABLE 2
X-RAY SPECTRAL FITTING MODELS

Model	XSPEC Components
Total	
M04a/b	tbabs*(pexrav+cutoffp1+zgauss(Fe _{neutral} , Fe _{ionized} , Ni _{neutral}))
M04c	tbabs*(MYTZ*cutoffp1+cutoffp1+pexrav+zgauss(Fe _{neutral} , Fe _{ionized} , Ni _{neutral}))
Nucleus Only	
P	tbabs(tbabs(MYTZ*cutoffp1+C _{RRC} +C _{RL} +pow+zedge(Ni)*gsmooth(pexmon)+zgauss(Ni K β)))
M1	tbabs(tbabs(MYTZ*cutoffp1+C _{RRC} +C _{RL} +pow+highcut*zedge(Ni)*MYTS+gsmooth*MYTL+zgauss(Ni _{neutral})))
M2	tbabs(tbabs(MYTZ*cutoffp1+C _{RRC} +C _{RL} +pow+highcut*zedge(Ni)*MYTS(0°, 90°)+gsmooth*MYTL(0°, 90°)+zgauss(Ni _{neutral})))
T	tbabs(tbabs(C _{RRC} +C _{RL} +pow+highcut+gsmooth(torus)))
Host Only	
P	tbabs(pcfabs(C _{RRC} +C _{RL} +pow+zedge(Ni)*gsmooth(pexmon)+zgauss(Ni K β)))
M1	tbabs(pcfabs(C _{RRC} +C _{RL} +pow+highcut*zedge(Ni)*MYTS+gsmooth*MYTL+zgauss(Ni _{neutral})))
M2	tbabs(pcfabs(C _{RRC} +C _{RL} +pow+highcut*zedge(Ni)*MYTS(0°, 90°)+gsmooth*MYTL(0°, 90°)+zgauss(Ni _{neutral})))
T	tbabs(pcfabs(C _{RRC} +C _{RL} +pow+highcut+gsmooth(torus)))

NOTE. — We denote Fe_{neutral} to signify the modeling of neutral Fe K α (6.40 keV) and K β (7.07 keV) transitions, while we use Ni_{neutral} for the modeling of neutral Ni K α (7.47 keV) and K β (8.23 keV) lines. We denote Fe_{ionized} to signify the modeling of ionized Fe K α H-like (6.97 keV), He-like (6.69 keV), and Be-like (6.57 keV) transitions. We denote C_{RRC} to signify the modeling of the radiative recombination continuum, which is modeled by a 0.3 keV brems component. We denote C_{RL} to signify the modeling of the radiative recombination line emission, which is comprised of numerous transitions from a variety of elements. We adopted line species, energies and strengths consistent with those reported in K14 (which includes Fe_{ionized}), as well as Ni He-like K α (7.83 keV). For the ACIS-S host spectrum, we model only a subset of lines comprising just the strongest handful of K14 lines.

range; this applies to the 3–10 keV range overall as well. Uncertainties in the normalization offsets between instruments, and hence flux differences, above 10 keV are considerably larger, making it more difficult to assess potential variability. Nonetheless, after accounting for known cross-calibration offsets, we find that the *NuSTAR*, *Suzaku* PIN, 1998 *BeppoSAX* PDS, and *Swift* BAT spectra above 10 keV are likewise consistent within their statistical uncertainties. The 1996 *BeppoSAX* PDS spectra, which lack the pronounced residuals around 30 keV that we observe from the other hard X-ray spectra, differ from the rest at marginal significance (2.5σ) and in fact appear to be relatively well-fitted by the fixed Matt et al. (2004) model ($\chi^2_\nu = 1.43$ for $\nu = 57$ by itself; perhaps this is no surprise since the model is based on these data). Here, it is important to remember that the *BeppoSAX* PDS, *Suzaku* PIN, and *Swift* BAT spectra are all strongly background-dominated (see §2.4–2.6), and minor variations in background levels (e.g., due to minor flares or how the data are screened) can potentially lead to large variations in the source spectra. The fact that we see an overall consistency in the spectral shape of the residuals, aside from the one discrepant point in the 1996 *BeppoSAX* PDS spectra around 30 keV, demonstrates that there has been no strong variability detected over at least the past ≈ 15 years.

We note that the χ^2 residuals are dominated by the *XMM-Newton* pn and *NuSTAR* spectra, and thus, for clarity, we opt to use only the *XMM-Newton* pn and combined FPMA/FPMB *NuSTAR* spectra to represent the global spectrum of NGC 1068 hereafter. To this end, we plot the unfolded *XMM-Newton* pn and composite *NuSTAR* spectra along with the various components that comprise the M04a model again in the left panel of Figure 3, as well as the data-to-model residuals. This fit yielded a reduced $\chi^2_\nu = 1.61$ for $\nu = 1234$. The continuum parameter values and errors are listed in Table 3, while the normalizations of the various lines are given in Table 4. For *NuSTAR*, the redshifts for the neutral and ionized lines were $-0.0065^{+0.0005}_{-0.0006}$ and $0.0081^{+0.0012}_{-0.0010}$, respectively, while for *XMM-Newton* they were $0.0015^{+0.0003}_{-0.0008}$ and $0.0026^{+0.0012}_{-0.0013}$, respectively.

Allowing the powerlaw index, high-energy cutoff, and Fe abundance and inclination angle of the reflector to vary, hereafter model “M04b”, improves the fit substantially, with a reduced $\chi^2_\nu = 1.20$ for $\nu = 1230$. As shown in Figure 3, most of

the residuals are now due to the Fe/Ni line complex with only very mild residuals seen from the Compton hump above 10 keV. The emission line parameters remained more or less constant, while the best fitted values of the other parameters are $\Gamma = 1.76^{+0.04}_{-0.09}$, $\theta_{\text{inc}} = 70^{+20}_{-7}$, $E_c = 108^{+19}_{-13}$ keV, and $Z_{\text{Fe}} = 6.8 \pm 0.4$. Parameter values and errors for model M04b are listed in Table 3.

Another possibility that could explain the spectrum is if the direct continuum is partially punching through above 20–30 keV, often called the “leaky” torus model, hereafter model “M04c”. Given the high column density needed to produce flux only above ~ 30 keV, we need to account properly for the effects of Compton absorption, which we do through the use of the multiplicative transmission component from the MYTORUS set of models (hereafter MYTZ to denote “zeroth-order” component; Murphy & Yaqoob 2009) and a cutoff power law (cutoffp1); see also §4.2. For this direct component, we tie the values of the intrinsic continuum slope, cutoff energy, and redshift to those of the scattered components, which were left to vary. The normalizations for the three continuum components were free to vary as well. The inclination angle and Fe abundance of the pexrav component of M04c were fixed at 63° and 2.4, respectively, as in M04a, to limit the number of free parameters. This model yields a reduced $\chi^2_\nu = 1.22$ for $\nu = 1227$, with most of the residuals due to the Fe line complex and only very mild residuals around the Compton hump above 10 keV. As before, the emission line parameters remained more or less constant, while the best fitted values of the other parameters are a photon index of $\Gamma = 1.92^{+0.05}_{-0.06}$, an exponential cutoff rollover energy of $E_c = 22^{+24}_{-9}$ keV, a column density for the absorbed transmission component of $N_{\text{H}} > 9.95 \times 10^{24}$ cm $^{-2}$, and normalizations of $A_{\text{trans}} = 67.8^{+2.5}_{-1.8}$ photons keV $^{-1}$ cm $^{-2}$ s $^{-1}$ at 1 keV, $A_{\text{warm}} = (7.9 \pm 0.5) \times 10^{-4}$ photons keV $^{-1}$ cm $^{-2}$ s $^{-1}$ at 1 keV, and $A_{\text{cold}} = (1.1^{+2.4}_{-1.8}) \times 10^{-2}$ photons keV $^{-1}$ cm $^{-2}$ s $^{-1}$ at 1 keV. Parameter values for model M04c are listed in Table 3.

Clearly the best-fitted M04a model fails to provide an adequate description of the *NuSTAR* data, while both of the alternative models, M04b and M04c appear to yield more reasonable fits. The Fe abundance constraints from M04b are substantially super-solar, which is consistent with past constraints on NGC 1068 (e.g., Kinkhabwala et al. 2002; Kraemer et al.

TABLE 3
MODEL SPECTRAL FIT PARAMETERS

(1) Model	(2) Spectra	(3) Range	(4) Γ	(5) N_{H}	(6) E_c	(7) θ_{inc}	(8) θ_{open}	(9) Z_{Fe}	(10) S/L ratio	(11) $\log F_{\text{X,cold}}$	(12) $\log F_{\text{X,warm}}$	(13) χ^2_{ν} (ν)
Total (Previous Models)												
M04a	XN	3–79	2.04	10	500	63	...	2.4*	...	-11.70 ^{+0.01} _{-0.01}	-11.67 ^{+0.01} _{-0.01}	1.61 (1234)
M04b	XN	3–79	1.76 ^{+0.04} _{-0.09}	10	108 ⁺¹⁹ ₋₁₈	70 ⁻ ₋₇	...	6.8 ^{+0.4*} _{-0.4}	...	-11.86 ^{+0.02} _{-0.02}	-11.57 ^{+0.01} _{-0.01}	1.20 (1230)
M04c	XN	3–79	1.92 ^{+0.05} _{-0.06}	10 ⁻ _{-0.05}	22 ⁺²⁴ ₋₉	63	...	2.4*	...	-11.74 ^{+0.01} _{-0.01}	-11.64 ^{+0.01} _{-0.01}	1.22 (1227)
Nucleus Only												
P	H	0.5–9	2.46 ⁻ _{-0.24}	10	500	85	...	4.5 ^{+1.1} _{-0.6}	...	-11.80 ^{+0.02} _{-0.02}	-11.75 ^{+0.04} _{-0.04}	1.60 (1472)
P	H	2–9	1.15 ^{+0.32} ₋	10	500	85	...	5.1 ^{+3.7} _{-0.9}	...	-11.79 ^{+0.12} _{-0.17}	-11.79 ^{+0.14} _{-0.22}	0.66 (319)
M1	H	0.5–9	1.40 ^{+0.12} ₋	10	500	90	60	...	0.42 ^{+0.12} _{-0.08}	-11.82 ^{+0.08} _{-0.05}	-11.81 ^{+0.02} _{-0.09}	1.64 (1472)
M1	H	2–9	1.40 ^{+0.16} ₋	10	500	90	60	...	0.46 ^{+0.13} _{-0.08}	-11.73 ^{+0.02} _{-0.07}	-11.87 ^{+0.10} _{-0.09}	0.72 (319)
M2	H	0.5–9	2.60 ⁻ _{-0.19}	10	500	0.90	60	...	0.67 ^{+0.09} _{-0.09}	-11.54 ^{+0.02} _{-0.02}	-12.36 ^{+0.14} _{-0.14}	1.62 (1471)
M2	H	2–9	1.52 ^{+0.01} _{-0.08}	10	500	0.90	60	...	0.64 ^{+0.13} _{-0.11}	-11.87 ^{+0.14} _{-0.11}	-11.76 ^{+0.03} _{-0.16}	0.74 (318)
T	H	0.5–9	1.30 ^{+0.09} _{-0.05}	10	...	87	67 ⁺¹² ₋₁₁	-11.78 ^{+0.03} _{-0.05}	-11.76 ^{+0.02} _{-0.02}	1.65 (1472)
T	H	2–9	1.14 ^{+0.33} ₋	10	...	87	67 ⁺¹⁵ ₋₁₇	-11.82 ^{+0.30} _{-0.09}	-11.69 ^{+0.02} _{-0.09}	0.73 (319)
Host Only												
P	A	0.5–9	2.49 ⁻ _{-0.19}	...	500	85	...	33 ⁺⁴⁰ ₋₁₃	...	-12.47 ^{+0.08} _{-0.11}	-12.09 ^{+0.04} _{-0.09}	1.42 (163)
P	A	2–9	2.49 ⁻ _{-0.40}	...	500	85	...	100 ⁻ ₋₆₀	...	-12.45 ^{+0.22} _{-0.22}	-12.11 ^{+0.09} _{-0.03}	0.81 (73)
M1	A	0.5–9	2.55 ⁻ _{-0.06}	10	500	90	60	...	2.46 ^{+3.49} _{-1.01}	-12.37 ^{+0.11} _{-0.16}	-12.11 ^{+0.03} _{-0.03}	1.44 (163)
M1	A	2–9	2.60 ⁻ _{-0.42}	10	500	90	60	...	2.27 ^{+0.38} _{-0.90}	-12.35 ^{+0.07} _{-0.38}	-12.12 ^{+0.10} _{-0.03}	0.89 (73)
M2	A	0.5–9	2.56 ⁻ _{-0.06}	10	500	0.90	60	...	2.25 ^{+2.65} _{-0.90}	-12.36 ^{+0.10} _{-0.15}	-12.11 ^{+0.04} _{-0.03}	1.44 (162)
M2	A	2–9	2.60 ⁻ _{-0.35}	10	500	0.90	60	...	2.70 ^{+5.20} _{-1.09}	-12.34 ^{+0.10} _{-0.33}	-12.13 ^{+0.10} _{-0.03}	0.87 (72)
T	A	0.5–9	2.61 ^{+0.06} _{-0.06}	10	...	87	26 ⁺¹³ ₋₂₆	-12.24 ^{+0.07} _{-0.08}	-12.17 ^{+0.03} _{-0.03}	1.49 (163)
T	A	2–9	2.91 ⁻ _{-0.39}	10	...	87	26 ⁺¹⁷ ₋₂₆	-12.17 ^{+0.07} _{-0.10}	-12.25 ^{+0.10} _{-0.17}	0.94 (73)
Total (Nucleus+Host Models)												
Pa	HAXNB	2–195	1.57 ^{+0.02} _{-0.02}	10	500	85	...	5.0 ^{+0.3} _{-0.3}	...	-11.87 ^{+0.02} _{-0.02}	-11.90 ^{+0.02} _{-0.10}	1.34 (1666)
M1a	HAXNB	2–195	1.40 ^{+0.09} ₋	10	500	90	1	-12.40 ^{+0.05} _{-0.05}	-12.60 ^{+0.10} _{-0.13}	3.78 (1666)
M1d	HAXNB	2–195	1.40 ^{+0.12} ₋	9.4 ⁻ _{-3.3}	41 ⁺⁵ ₋₄	78 ⁺³ ₋₄	3.8 ^{+0.5} _{-0.8}	-14.00 ^{+0.30} _{-0.03}	-11.92 ^{+0.03} _{-0.03}	1.31 (1662)
M1g	HAXNB	2–195	1.40 ^{+0.34} ₋	10	34 ⁺⁵⁸ ₋₄	80.7 ^{+6.5} _{-3.4}	-13.33 ^{+0.14} _{-0.22}	-11.99 ^{+0.02} _{-0.02}	1.29 (1660)
M2a	HAXNB	2–195	2.29 ^{+0.04} _{-0.02}	10	500	90	1	-12.05 ^{+0.01} _{-0.01}	-12.83 ^{+0.17} _{-0.29}	1.83 (1666)
M2d	HAXNB	2–195	2.10 ^{+0.06} _{-0.07}	10.0 ⁻ _{-0.3}	128 ⁺¹¹⁵ ₋₄₄	90	1.0 ^{+0.1} _{-0.1}	-11.87 ^{+0.01} _{-0.02}	-12.10 ^{+0.02} _{-0.02}	1.83 (1666)
Ta	HAXNB	2–195	1.96 ^{+0.05} _{-0.04}	10	500	87	64 ⁺³ ₋₂	-13.90 ^{+0.25} _{-0.60}	-12.08 ^{+0.02} _{-0.02}	1.14 (1666)
Tc	HAXNB	2–195	2.13 ^{+0.04} _{-0.06}	6.3 ^{+0.6} _{-0.8}	500	87 ⁻ ₋₁₂	69 ⁺⁴ ₋₃	...	1	-12.92 ^{+0.03} _{-0.03}	-12.34 ^{+0.05} _{-0.05}	1.14 (1666)
				10						-12.36 ^{+0.04} _{-0.05}	-12.20 ^{+0.03} _{-0.03}	1.61 (1667)
				5.0 ^{+4.2} _{-1.9}						-11.95 ^{+0.02} _{-0.03}	-11.86 ^{+0.02} _{-0.02}	1.61 (1667)
				10						-14.00 ^{+0.30} ₋	-11.92 ^{+0.03} _{-0.03}	1.57 (1663)
				10 ⁻ _{-6.6}						-11.96 ^{+0.02} _{-0.03}	-11.87 ^{+0.02} _{-0.02}	1.57 (1663)
										-14.00 ^{+0.30} ₋	-11.92 ^{+0.03} _{-0.03}	

NOTE. — *Column 1*: Model used. Model name beginning with “M04” denote variations of M04 models; “P” denote variations of *pexmon* models; “M1” denote variations of coupled *MYTORUS* models; “M2” denote variations of decoupled *MYTORUS* models; “T” denote variations of *Torus* models. See §4.1 and §4.2 for details. When multiple rows are listed, the first one or two rows represent the nucleus model while the second or third row represents the host model. *Column 2*: Spectra fit, where X=*XMM-Newton* pn, A=*Chandra* ACIS-S, H=*Chandra* HEG+MEG, N=*NuSTAR*, and B=*Swift* BAT. *Column 3*: Energy range fit, in keV. *Column 4*: Photon index of the primary transmitted powerlaw continuum. Note that some reported limits are poorly constrained since the allowed ranges for Γ are confined to between 1.1–2.5 for the *pexmon* model, between 1.4–2.6 for the *MYTORUS* model, and between 1–3 for the *Torus* model. *Column 5*: Neutral hydrogen column density of the obscuring torus/clouds, in units of 10^{24} cm^{-2} . *Column 6*: Energy of the exponential cutoff rollover of primary transmitted powerlaw continuum, in keV. *Column 7*: Inclination angle with respect to a face-on geometry, in degrees. Note that some reported limits are poorly constrained since the allowed ranges for θ_{inc} are confined to 0° – 72° for the M04 (*pexrav*) model, 0° – 85° for the *pexmon* model, and 18° – 87° for the *Torus* model. *Column 8*: Torus opening angle, in degrees. This parameter is not meaningful for the M04 and *pexmon* models, is fixed at 60° for the *MYTORUS* model, and is confined to 25° – 84° for the *Torus* model. *Column 9*: Fe abundance with respect to our adopted value of $Z_{\odot, \text{Fe}}$. The overall abundance of metals (not including Fe) is assumed to be solar (Z_{\odot}). Note that entries denoted by * are for *pexrav*, where the Fe abundance is driving the peak of the Compton reflection hump to higher energy and has no effect on the Fe line emission, which is modeled with Gaussians. *Column 10*: Ratio of the scattered and line components of *MYTORUS*. This can crudely be interpreted as an Fe abundance with respect to our adopted value of $Z_{\odot, \text{Fe}}$, although care should be taken since the correspondence is non-trivial and hence only approximate (Yaqoob 2012). *Columns 11–12*: Logarithms of the 2–10 keV fluxes of the cold and warm reflection components, respectively, in units of $\text{erg s}^{-1} \text{ cm}^{-2}$. *Column 13*: Reduced χ^2_{ν} and degrees of freedom for given model. Values with no quoted errors were fixed at their specified values.

TABLE 4
FE AND NI LINE FLUXES (WITH MODEL M04B)

Line	<i>XMM-Newton</i>		<i>Chandra</i>	
	M04 <40''	this work <75''	HETG <2''	ACIS-S 2''-75''
Fe neutral K α	44.3	47.4 ^{+1.9} _{-2.2}	38.9 ^{+3.8} _{-3.8}	17.5 ^{+3.3} _{-3.3}
Fe neutral K α CS	8.7	3.8 ^{+1.5} _{-2.2}	4.2 ^{+3.6} _{-2.2}	< 1.5
Fe neutral K β	9.1	8.9 ^{+1.1} _{-1.5}	4.3 ^{+3.1} _{-1.9}	< 5.2
Ni neutral K α	5.6	5.8 ^{+1.3} _{-0.9}	< 7.3	< 8.8
Ni neutral K β	3.2	3.1 ^{+0.9} _{-1.3}	< 19.8	< 16.8
Fe Be-like 6.57 keV	7.6*	8.0 ^{+1.5} _{-2.1}	6.3 ^{+2.1} _{-2.5}	3.9 ^{+2.9} _{-2.9}
Fe He-like 6.69 keV	22.8*	27.8 ^{+1.0} _{-2.9}	12.8 ^{+3.9} _{-2.3}	6.1 ^{+2.4} _{-2.4}
Fe H-like 6.97 keV	7.1*	8.2 ^{+0.8} _{-2.5}	7.7 ^{+1.5} _{-5.8}	< 6.1
Ni He-like 7.83 keV	2.7*	3.9 ^{+1.1} _{-1.1}	< 10.2	< 10.4

NOTE. — *Column 1*: Primary Fe and Ni lines measured in M04 and here using the *XMM-Newton* and *Chandra* datasets. The continuum was fit in all cases with the M04b model for consistency. *Columns 2-5*: Normalizations of the best-fitted *zgauss* components to each line, in units of 10^{-6} photons $s^{-1} cm^{-2}$. The components denoted by *'s were mistakenly listed in Table 3 of M04 with values a factor of 10 higher than intended (G. Matt, private communication); they have been corrected here for clarity. The difference between *XMM-Newton* pn values is at least partially due to differences in encircled energy fractions (87% vs. 93%) between the extraction regions.

1998) as well as some unobscured AGN (e.g., Fabian et al. 2009, 2013; Parker et al. 2014), although such results are not necessarily definitive. The overabundance is at least partially driven by the need to fit the 30 keV bump with a much deeper iron edge. Thus model M04b remains potentially viable. Model M04c provides an equally acceptable fit, although it requires that the transmitted component dominates above 20 keV with rather unusual best-fit parameters. For instance, the cutoff energy implies a unrealistically low corona temperature (e.g., Petrucci et al. 2001), while the ratio of transmitted-to-scattered normalizations is abnormally high (≈ 6000). As such, this scenario seems unlikely on its own and can be further ruled out by the variability constraints presented in §2.1 and §2.6, which imply that NGC 1068 is more or less constant over all of the timescales which we have measured.

One might be tempted to stop here, having modeled the global *NuSTAR* and *XMM-Newton* spectra to a reasonably acceptable level. However, higher spectral and angular resolution data from *Chandra* exist, allowing us to remove potential host contamination and thus probe the nature of the scattering medium in more detail. Additionally, a critical drawback of the *pexrav* model, for instance, is that it models a simple slab-like geometry for the Compton scatterer assuming an infinite column density, which almost certainly fails to adequately describe the true physical situation (e.g., a smooth or clumpy torus) present in NGC 1068. To this end, we also explore a variety of models which adopt more realistic geometrical scenarios for AGN scattering in section §4.2.

4.2. Detailed Spectral Modeling

At this point, it is critical to define which spectral models we will fit to the data, as there are a variety of models of Compton-scattered emission which have been used to fit reflection-dominated spectrum to account for the possible different geometries of the scattering material. These include

- *pexmon* — this is a modified version of the standard *pexrav* model (Magdziarz & Zdziarski 1995) already used in §4.1, which self-consistently computes the con-

tinuum (based on *pexrav*) as well as the neutral Fe K α , Fe K β and Ni K α emission lines (based on Monte Carlo simulations by George & Fabian 1991) and the Fe K α Compton shoulder (Nandra et al. 2007). As with *pexrav*, this model assumes that the scattering structure has a slab geometry and infinite optical depth. Moreover, the total and Fe abundances can be adjusted to account for non-solar values. The Ni edge is not included in this model, so we add this as a zedge component at the systemic redshift, the depth of which is tied to the the measured Ni K α flux (a value of $\tau = 0.1$ in zedge achieved this). Results for the series of *pexmon* Compton scattering models are detailed below and summarized in Table 3. We caution that the *pexmon* model is limited to photon indices between $\Gamma = 1.1-2.5$ and inclination angles $\theta = 0^\circ-85^\circ$.

- *MYTORUS* — functions for a smoothly distributed toroidal reprocessor composed of gas and dust with finite optical depth and with a fixed 60° opening angle (Murphy & Yaqoob 2009). *MYTORUS* is comprised of three separate spectral components: a transmitted intrinsic continuum component (*MYTZ*, incorporated as a multiplicative table) which represents the photons along the direct line of sight to the nucleus which remain after scattering, and Compton-scattered continuum (hereafter *MYTS*) and fluorescent line and Compton shoulder (hereafter *MYTL*) components which represent photons scattered into our line of sight from a different viewing angle to the nucleus (both additive table models). The neutral Fe lines are modeled self-consistently with the Compton-scattered component. By using multiple scatterers, varying their relative normalizations and/or inclination angles with respect to our line of sight, disentangling their column densities, and so forth, Yaqoob (2012) demonstrated that one could model a wide range of possible geometries surrounding the central engine. The Ni edge is not included in this model, so we must add this as a zedge component at the systemic redshift, the depth of which is tied to the measured Ni K α flux (which empirically equates to fixing $\tau = 0.1$). The model does not allow dynamic fitting for a high-energy cutoff, and table models are only computed for a handful of fiducial “termination” energies (E_T , which effectively is an instant cutoff).³³ For expediency, we chose to implement a dynamic cutoff separately using the $E_T = 500$ keV model multiplied by the *higecut* model with a fixed pivot energy of 10 keV and an e-folding energy that is tied to the transmitted powerlaw cutoff energy.³⁴

³³ Below energies of ≈ 20 keV, the *MYTORUS* models with different termination energies are virtually identical, while above this value the lower termination energy models have pseudo-exponential cutoffs, the forms of which depend modestly on input parameters. Using a sharp termination compared to an exponential cutoff should lead to mild differences in the shape of the cutoff. Unfortunately, the lack of any continuum above the termination energy imposes parameter limitations when fitting, e.g., the *Swift* BAT spectrum. While there may be merits to the arguments given in the *MYTORUS* manual against applying a cutoff, we find the alternative, a dramatic cutoff, to also be unsatisfactory from a physical standpoint.

³⁴ While applying exponential cutoffs outside of *MYTORUS* is expressly warned against in the *MYTORUS* manual, we found that this method yielded reasonable consistency compared to the various *MYTORUS* termination energy models over the ranges of parameters we fit, such that constraints on the cutoff energies typically were less than a factor of two different from the termination energy considered.

It is argued in the MYTORUS manual that applying a high-energy cutoff ruins the self-consistency of the MYTORUS; therefore, once we determined an approximate E_{cut} for our best-fit model, we dropped the use of `highcut` and replaced the $E_T = 500$ keV model with one which best approximates $E_{\text{cut}} = E_T$. Results for the series of MYTORUS Compton scattering models are detailed below and summarized in Table 3. We caution that the MYTORUS model is computed only for photon indices between $\Gamma = 1.4$ – 2.6 , to energies between 0.5 – 500 keV, and solar abundances.

- `torus` — this model describes obscuration by a spherical medium with variable N_{H} and inclination angle, as well as a variable biconical polar opening angle (Brightman & Nandra 2011). `torus` self-consistently predicts the $K\alpha$ and $K\beta$ fluorescent emission lines and absorption edges of all the relevant elements. The key advantage of this model is it can fit a range of opening angles and extends up to $N_{\text{H}} = 10^{26}$ cm², but a major drawback is that it does not allow the user to separate the transmitted and Compton-scattered components. As such, it can only be applied to the nuclear emission and is not appropriate to model the host component, which should include only the Compton-scattered emission. As with MYTORUS, `torus` does not allow dynamic fitting for a high-energy cutoff, so we implemented a cutoff using `highcut` in the same manner as for MYTORUS. Results for the series of `torus` Compton scattering models are detailed below and summarized in Table 3. We caution that the `torus` model is limited to photon indices between $\Gamma = 1.0$ – 3.0 , inclination angles $\theta_{\text{inc}} = 18^\circ$ – 87° , opening angles $\theta_{\text{tor}} = 25^\circ$ – 84° , and solar abundances.

Both MYTORUS and `torus` provide significant and distinct improvements over the geometric slab model which manifest in the spectral shapes of both line and continua. Nonetheless, the reader should keep in mind that they too only sample a small portion of the potential parameter space that likely describes real gas distributions in the vicinity of AGN. As done in §4.1, we model the transmitted powerlaw continuum as `MYTZ*cutoffpl` where applicable.

Before we proceed to fitting these more complex models, we note that while *NuSTAR* and *XMM-Newton* have large collecting areas and wide energy coverage, neither is able to spatially separate the spectra of the AGN from various sources of host contamination (or even extended AGN emission from point-like AGN emission), nor are they able to spectrally resolve some line complexes to gain a better understanding of the physical processes involved (Kinkhabwala et al. 2002, e.g., K14;). We rely on the *Chandra* data for these purposes, allowing us to construct the most robust model to date for the nuclear and global spectra of NGC 1068. We use the *Chandra* HETG spectra to model the point-like nuclear emission from NGC 1068 from the inner $2''$ in §4.2.1 and use the *Chandra* ACIS-S data to model the host galaxy emission from NGC 1068 between 2 – $75''$ in §4.2.2, both of which are fit between 0.5 – 9.0 keV. Fitting down to 0.5 keV allows us to constrain the soft-energy components, which can affect the flux and slope of the ionized reflector if unaccounted for. We then proceed to fit the combination of the nuclear and host galaxy emission to the *NuSTAR*, *XMM-Newton*, and *Chandra* spectra in §4.2.4. We also fit the *Swift* BAT spectra with this combined

spectrum, since the BAT spectrum provides some additional spectral coverage up to ≈ 200 keV and its spectral shape more or less agrees with *NuSTAR* where the two spectra overlap (see Figure 2).

4.2.1. Point-Like Nuclear Emission

The HETG nuclear spectra are shown in Figure 6, and clearly exhibit emission from several different components. To reproduce the main features of the HETG spectra, we assume that the nucleus AGN spectrum has a direct transmitted power law (`cutoffpl`) with slope Γ_{nuc} and cutoff energy $E_{\text{c,nuc}}$, which is absorbed by a presumably Compton-thick absorber (e.g., an edge-on torus) with neutral column density N_{H} (modeled as `MYTZ*cutoffpl`). Based on the modeling in §4.1, we adopt fixed values of $N_{\text{H}} = 10^{25}$ cm² and $\theta_{\text{inc}} = 90^\circ$ for the absorber; these quantities are poorly constrained by the < 10 keV data alone due to degeneracies with other spectral components (see below). Although the transmitted component is not observable below ~ 10 keV (if at all) in Compton-thick AGN, most of the observed < 10 keV features should be indirect products of it.

We empirically model the soft RRC and RL emission as a bremsstrahlung component (`brems`, best-fit $kT_{\text{brems}} = 0.31 \pm 0.03$ keV and $A_{\text{brems}} = 0.013 \pm 0.01$ cm²) and ≈ 90 narrow ionized emission lines (`zgauss`), respectively. The latter are based on the line identifications from K14 plus Ni He-like 7.83 keV. For simplicity we adopt a single redshift z_{ion} and line width σ_{ion} (fixed at 0.0035 keV) for the vast majority of the ionized lines. The line normalizations are in crude agreement with K14, although there are differences due to our adopted widths and redshifts; as these are primarily used so that we can constrain the RRC `brems` temperature and normalization, we do not report the line properties here. Even with all of these components, significant complex Fe and Si line emission remains (see Figure 6; residuals can also be seen in Figures 1–4 of K14), which we modeled empirically as a broad $\sigma = 0.2$ keV line centered at 6.69 keV and a broad $\sigma = 0.1$ keV line centered at 2.38 keV, respectively, which reduced the residuals significantly.

The hard X-ray emission is modeled with a “warm” scattered powerlaw reflector and a “cold” Compton-scattered continuum plus emission lines. For the former component, we naively adopt a power law with the same intrinsic slope as the obscured transmitted component.³⁵ For the latter component, we adopt either `pexmon`, MYTORUS, or `torus`, as described above, none of which is particularly well-constrained by the *Chandra* HETG data alone. All of the cold reflection models were smoothed with an 0.01 keV Gaussian to best-match the HETG neutral Fe $K\alpha$ line width. We added neutral Ni $K\alpha$ (7.47 keV) and/or $K\beta$ (8.23 keV) lines when these were not modeled explicitly by the cold reflection models; these lines are poorly constrained by the HETG spectra, and thus were fixed relative to the full extraction region values from *XMM-Newton* assuming a nuclear to galaxy ratio of 2:1 as found for

³⁵ This warm mirror gas in NGC 1068 is possibly the same warm absorber gas seen in many Seyfert 1s (e.g., K14), in which case the ionization level of the gas is not sufficiently high to be a perfect mirror. As noted in §1, this could imprint significant absorption edges/lines on the spectrum up to several keV (e.g., Kaspi et al. 2002), effectively adding spectral curvature, primarily below 2 keV, or flattening the slope of this component. We tested the possible effects of this modification on our results using an ionized absorber produced by *XSTAR* for NGC 3227 (see Markowitz et al. 2009, for details). The primary effect was an increase in the normalization of the RRC component, with little change to the parameters of the components which dominate above 2 keV. Given this outcome, we chose a perfect mirror for simplicity.

neutral Fe $K\alpha$ (see §4.2.3). Similar to the transmitted component, we fixed the reflection component inclination angle to $\theta_{\text{inc}} = 90^\circ$, which is close to the nominal viewing angle associated with NGC 1068, and the high-energy exponential cut-off rollover energy to $E_c = 500$ keV for all models. Finally, we included two neutral absorption (tbabs) components, one of which was fixed at the Galactic column while the other was fit as $N_{\text{H}} = (1.5^{+0.2}_{-0.1}) \times 10^{21}$ cm $^{-2}$ to constrain the host column density in NGC 1068.

We now proceed to fit the cold reflection with various prescriptions. For all of the models below, we list the best-fit parameter values in Table 3 (“Nucleus Only”) and show the resulting data-to-model residuals in Figure 6. Fitting the `pexmon` model (model P in Table 2) yielded a reduced $\chi^2_\nu = 1.60$ for $\nu = 1471$ in the 0.5–9 keV range. The best-fit redshifts for the neutral and ionized lines were 0.00392 ± 0.0004 and 0.00371 ± 0.00008 , respectively, while the best-fit powerlaw index, Fe abundance, and normalizations were $\Gamma = 2.46^{+0.24}_{-0.6}$, $Z_{\text{Fe}} = 4.5^{+1.1}_{-0.6}$, $A_{\text{cold}} = (8.9^{+5.0}_{-0.5}) \times 10^{-2}$ photons keV $^{-1}$ cm $^{-2}$ s $^{-1}$ at 1 keV, and $A_{\text{warm}} = (2.8 \pm 0.2) \times 10^{-4}$ photons keV $^{-1}$ cm $^{-2}$ s $^{-1}$ at 1 keV, respectively. The powerlaw slope is poorly constrained due to parameter limitations of the `pexmon` model.

We also fit the cold reflection with the `MYTORUS` model in two distinct configurations (models M1 and M2 in Table 2). The first (M1) is a standard coupled configuration, wherein the neutral hydrogen column densities N_{H} , intrinsic powerlaw slopes Γ , inclination angles θ_{inc} , and normalizations of the MYTZ (A_{pow}), MYTS (A_{MYTS}), and MYTL (A_{MYTL}) components are tied and fit together self-consistently to model a uniform torus geometry. The second (M2) is a decoupled configuration which employs two Compton scatterers, one edge-on and one face-on, where the corresponding normalizations for the different angles (e.g., $A_{\text{MYTS},90}$ and $A_{\text{MYTS},00}$) vary independently but the continuum and line components of a given angle are fixed as in model M1. This corresponds to a patchy torus whereby a portion of the Compton-scattered photons which “reflect” off the facing side of background clouds can bypass clouds which obscure photons along our direct line of sight (more details can be found in Yaqoob 2012, and we refer interested readers particularly to their Figure 15).

Fitting model M1 yielded a reduced $\chi^2_\nu = 1.64$ for $\nu = 1472$ in the 0.5–9 keV range. The best-fit redshifts for the neutral and ionized lines were 0.00391 ± 0.0004 and 0.00373 ± 0.00008 , respectively, while the best-fit powerlaw index, scattering-to-line component (S/L) ratio,³⁶ $\Gamma = 1.40^{+0.12}_{-0.08}$, S/L ratio = $0.42^{+0.12}_{-0.08}$, $A_{\text{MYTS,cold}} = 7.4^{+2.9}_{-1.8}$ photons keV $^{-1}$ cm $^{-2}$ s $^{-1}$ at 1 keV, and $A_{\text{warm}} = (2.63 \pm 0.3) \times 10^{-4}$ photons keV $^{-1}$ cm $^{-2}$ s $^{-1}$ at 1 keV, respectively. Meanwhile, model M2 yielded a reduced $\chi^2_\nu = 1.62$ for $\nu = 1471$ in the 0.5–9 keV range, best-fit powerlaw index, scattering-to-line component ratio, and normalizations were $\Gamma = 2.60^{+0.01}_{-0.19}$, S/L ratio = 0.67 ± 0.09 , $A_{\text{MYTS},00} = 0.19^{+0.01}_{-0.07}$ photons keV $^{-1}$ cm $^{-2}$ s $^{-1}$ at 1 keV, $A_{\text{MYTS},90} = 0.00^{+1.74}_{-0.07}$ photons keV $^{-1}$ cm $^{-2}$ s $^{-1}$ at 1 keV, and $A_{\text{warm}} = (4.1 \pm 0.2) \times 10^{-4}$ photons keV $^{-1}$ cm $^{-2}$ s $^{-1}$ at 1 keV, respectively. As before, the powerlaw slope is not very well-constrained over this particular energy range due to parameter limitations of the `MYTORUS` model.

Finally, we fit the cold reflection with the `TORUS` model (model T in Table 2). The best fit yielded a reduced $\chi^2_\nu =$

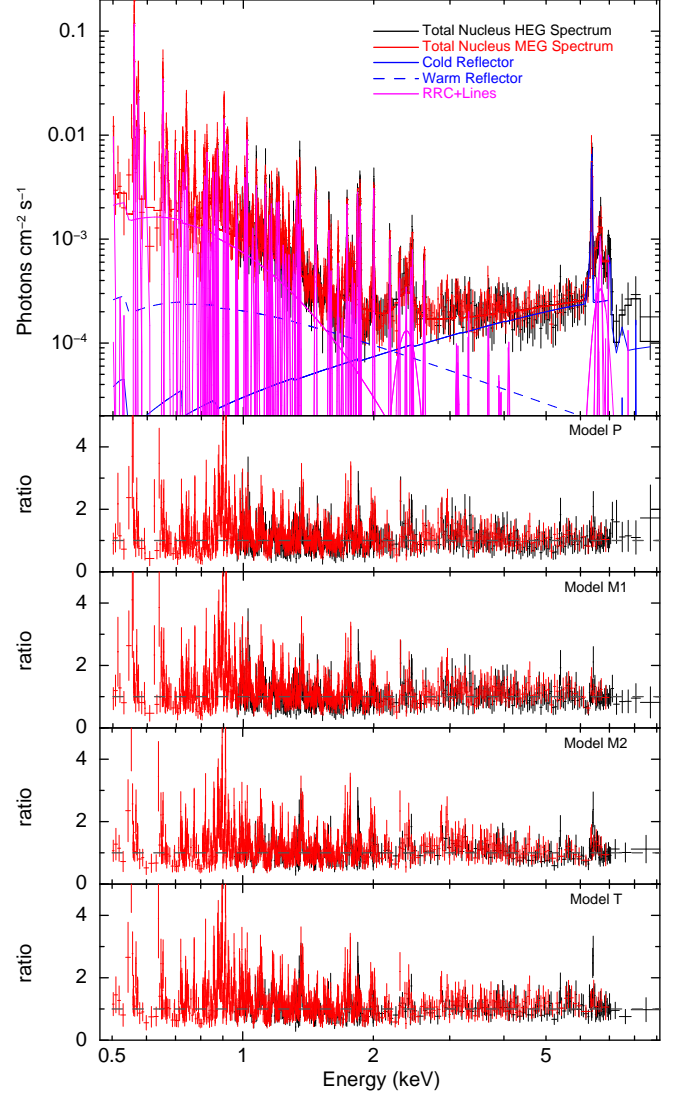


FIG. 6.— HEG (black) and MEG (red) unfolded spectra of nucleus of NGC 1068 extracted from a 4” full-width mask. The spectra are fitted with four models comprised of partially absorbed cold and warm reflectors (blue solid and dashed lines, respectively), as well as RRC and line components as identified by K14 (magenta solid lines). The top panel shows the fit to model P while the rest of the panels show the data-to-model ratios for models P, M1, M2, and T, respectively.

1.65 for $\nu = 1472$ in the 0.5–9 keV range. The best-fit redshifts for the neutral and ionized lines were $0.00363^{+0.0004}_{-0.0003}$ and $0.00370^{+0.00009}_{-0.00007}$, respectively, while the best-fit powerlaw index, opening angle, and normalizations were $\Gamma = 1.30^{+0.09}_{-0.05}$, $\theta_{\text{open}} = 67^{+12}_{-15}$ deg, $A_{\text{cold}} = (2.6^{+0.8}_{-0.5}) \times 10^{-2}$ photons keV $^{-1}$ cm $^{-2}$ s $^{-1}$ at 1 keV, and $A_{\text{warm}} = (3.0 \pm 0.2) \times 10^{-4}$ photons keV $^{-1}$ cm $^{-2}$ s $^{-1}$ at 1 keV, respectively. We note that the relatively low Γ value and small errors are largely dictated by the Fe lines, since there is no way to change the Fe line to continuum ratio through a metallicity parameter for this model.

As can be seen from Figure 6 and Table 3, all of the models are able to fit the 0.5–9 keV nucleus spectra equally well, with only very mild deviations in the residuals between them. In all cases, the residuals are almost exclusively due to low-level line emission (i.e., the strong ratio outliers in the lower pan-

³⁶ I.e., the ratio of the A_{MYTS} to A_{MYTL} normalizations.

els of Figure 6), most of which is below 2 keV, that remains unaccounted for despite modeling ≈ 90 emission lines. We found that these residuals bias the relative normalization of the `bremss` component downward by $\approx 20\%$, but do not appear to significantly affect the `bremss` temperature nor normalizations of the higher energy components (this holds for all of the cold reflection models). Notably, there are wide variations in the powerlaw slopes between models, which should be constrained better upon incorporating the >10 keV data. If we limit the fit to the 2–9 keV spectra and fix the `bremss` and `tbabs` components, the reduced χ^2_ν values drop to ≈ 1 and the photon indices become significantly harder ($\Gamma \approx 1.4$ – 1.5) in all cases, leading to decreased fractional contributions from the cold reflection in the 2–10 keV band. In the case of model M2, the 2–9 keV fit led to a reversal in the dominant cold reflection component from 0° to 90° . These large swings primarily demonstrate that the spectral properties of the cold and warm reflection are poorly constrained by the <10 keV data alone, even when high signal-to-noise and well-resolved emission lines can be fit.

4.2.2. Diffuse Emission and Point Source Contamination From Host Galaxy

Both extended and off-nuclear point source emission are evident in the *Chandra* images, particularly along the direction of the AGN radio jet and counter jet (see Figure 1). We modeled this emission in the *Chandra* ACIS-S data with several components to reproduce the main features in the galaxy, noting in particular that there are several key spectral signatures present in the nuclear spectra which are also prevalent in the host spectrum.

First, we include in the host galaxy model an absorbed power law with slope Γ_{pnt} to account for the combined emission from extranuclear point sources, which we constrain separately below. A composite *Chandra* ACIS-S spectrum of all of the point sources together is shown in Figure 7 (green data and model). There are some notable bumps in the soft portion of the spectrum, which could either be intrinsic or more likely are produced by poor background subtraction due to an inhomogenous extended emission component. As such, we fitted this spectrum only above 1.5 keV with a single cut-off powerlaw model. Unfortunately, the limited 0.5–9 keV energy range is not sufficient to unambiguously determine the average spectrum slope, high-energy cutoff, and normalization of the host galaxy point-source population. Following Swartz et al. (2004) and Walton et al. (2011), we assume that NGC 1068 hosts an ultraluminous X-ray source (ULX) population and that emission characteristic of this population likely dominates the point source emission. Recent evidence from *NuSTAR* (e.g., Bachetti et al. 2013; Rana et al. 2014; Walton et al. 2013, 2014) suggests that ULXs exhibit relatively hard spectra with spectral turnovers between 6–8 keV, and thus we adopt fixed values of $\Gamma = 1.2$ and $E_c = 7$ keV to represent the composite ULX-like spectrum. With these values, the normalization of the power law is 8.9×10^{-5} photons $\text{keV}^{-1} \text{cm}^{-2} \text{s}^{-1}$ at 1 keV. This component makes only a relatively small contribution to the overall host contamination in the 1.5–9.0 keV ($\approx 25\%$) range and quickly becomes negligible above 15 keV. We fixed the normalization of this fit and added this fixed off-nuclear point-source component to the overall host model.

At soft energies, we still see signs of extended RRC and line emission, which we again model as a $kT_{\text{bremss}} = 0.31^{+0.01}_{-0.01}$ keV

bremstrahlung component (`bremss`, $A_{\text{bremss}} = 0.0168^{+0.0004}_{-0.0003} \text{cm}^{-2}$) plus a subset of the 20 strongest emission lines found in the nuclear spectra; at the spectral resolution of ACIS-S, these 20 lines were sufficient to model nearly all of the spectral deviations from a smooth continuum. There may also be a contribution from hot gas associated with star formation, but since our main focus is to derive an empirical model to describe the soft emission, we simply absorb this into the normalization for the bremstrahlung plus line emission model. The character of the ionized lines differs from those found in the nucleus spectrum, in the sense that lower ionization line species such as S, Si, Mg are stronger in the host spectra relative to the ionized Fe lines, as might be expected for a UV/X-ray radiation field which is radiating from the central SMBH.

At hard energies, we additionally see traces of warm and cold AGN reflection as extended emission, which we model as a scattered power law and Compton-scattered continuum plus neutral lines, respectively. We continue to model the latter with either the `pexmon` or `MYTS+MYTL`; we do not fit the `torus` model, since one cannot explicitly separate out the transmitted component.³⁷ As before, we will assume that the warm and cold reflection components result from the scattering of the same direct transmitted power law (`cutoffpl`) with slope Γ_{nuc} and exponential cutoff rollover energy $E_{c,\text{nuc}}$, which is absorbed along the line of sight by a Compton-thick absorber (e.g., an edge-on torus). As before, we fixed the quantities $E_{c,\text{nuc}} = 500$ keV, $\theta_{\text{inc}} = 90^\circ$ and $N_{\text{H}} = 10^{25} \text{cm}^{-2}$, since these are poorly constrained by the <10 keV data alone.

Finally, we note that the absorption toward the counter-jet region is significantly stronger than that toward the jet region, so we initially fit all the components to the jet and counter-jet regions, allowing only for the N_{H} of the cold absorber to vary between them. This fit produced $N_{\text{H}} = 3.1 \times 10^{20} \text{cm}^{-2}$ toward the jet, consistent with the Galactic column, and $N_{\text{H}} = 2.4 \times 10^{21} \text{cm}^{-2}$ toward the counter jet. As such, the 2–75'' host region was modeled through a layer of cold Galactic absorption (`tbabs`) and a cold partial coverer (`pcfabs`) with $N_{\text{H}} = 2.4 \times 10^{21} \text{cm}^{-2}$ and covering fraction of 50%. For all of the models, we list the best-fit parameter values in Table 3 (“Host Only”) and show the resulting data-to-model residuals in Figure 7.

Fitting the `pexmon` (P) version of our host model yielded a reduced $\chi^2_\nu = 1.42$ for $\nu = 163$ in the 0.5–9 keV range. Given the quality and spectral resolution of the ACIS-S spectrum, we fixed the redshift at 0.00379. The best-fit powerlaw index, Fe abundance, and normalizations were $\Gamma = 2.49^{+0.25}_{-0.25}$, $Z_{\text{Fe}} = 43^{+19}_{-19}$, $A_{\text{cold}} = (2.5^{+0.4}_{-0.5}) \times 10^{-2}$ photons $\text{keV}^{-1} \text{cm}^{-2} \text{s}^{-1}$ at 1 keV, and $A_{\text{warm}} = (6.7 \pm 0.2) \times 10^{-4}$ photons $\text{keV}^{-1} \text{cm}^{-2} \text{s}^{-1}$ at 1 keV, respectively. It is worth noting here that the abundance value, albeit poorly constrained, is exceptionally high and probably highlights a critical breakdown of the model in this regime rather than an extreme intrinsic value. We also fit the host spectrum with the `MYTORUS` (M1 and M2) versions of our host model. Fitting model M1 produced a reduced $\chi^2_\nu = 1.44$ for $\nu = 163$ in the 0.5–9 keV range. The best-fit powerlaw index, scattering-to-line component ratio, and normalizations were $\Gamma = 2.55^{+0.06}_{-0.06}$, S/L ratio of $2.46^{+3.49}_{-1.01}$, $A_{\text{MYTS,cold}} = 1.2^{+0.8}_{-0.7}$ photons $\text{keV}^{-1} \text{cm}^{-2} \text{s}^{-1}$ at

³⁷ The `torus` transmitted component could be made negligible by increasing the column density to 10^{26}cm^{-2} , but this would mean we would have to model all clouds as extremely Compton-thick, which is a major limitation.

1 keV, and $A_{\text{warm}} = (6.8 \pm 0.2) \times 10^{-4}$ photons keV $^{-1}$ cm $^{-2}$ s $^{-1}$ at 1 keV, respectively. Meanwhile, model M2 yielded a reduced $\chi^2_{\nu} = 1.46$ for $\nu = 162$ in the 0.5–9 keV range, best-fit powerlaw index, scattering-to-line component ratio, and normalizations were $\Gamma = 2.56_{-0.05}^{+0.05}$, S/L ratio of $2.25_{-0.90}^{+2.65}$, $A_{\text{MYTS},00} = (1.7_{-1.1}^{+1.1}) \times 10^{-2}$ photons keV $^{-1}$ cm $^{-2}$ s $^{-1}$ at 1 keV, $A_{\text{MYTS},90} = 0.00_{-1.58}^{+1.58}$ photons keV $^{-1}$ cm $^{-2}$ s $^{-1}$ at 1 keV, and $A_{\text{warm}} = (6.7 \pm 0.2) \times 10^{-4}$ photons keV $^{-1}$ cm $^{-2}$ s $^{-1}$ at 1 keV, respectively. We note that the reflection component from the host emission should be comprised almost exclusively of inclination 0° (“far-side, face-on”) reflection spectra whose line-of-sight does not intercept any torus material (see further discussion in Yaqoob 2012); thus we can effectively neglect the 90° component altogether.

Similar to the nucleus fits, the powerlaw slopes for models P, M1, and M2 were not well-constrained due to parameter limitations of the various models and data bandpass limitations. The bulk of the residuals arise from unaccounted-for line emission below 2 keV. As seen in Table 3, when we fit the models to the >2 keV spectrum and fix the bremsstrahlung component, the reduced χ^2_{ν} values drop considerably for all models.

4.2.3. Empirical Constraints on Extended Fe Line Emission

An alternative, more empirical approach can be made to understand the contribution from extended cold and warm reflection. For this, we simply measure the line fluxes from the two strongest tracers, the fluorescent Fe K α line and the ionized Fe He-like line, respectively. For simplicity, we use the M04a model (although we replace `pexmon` by `pexrav` in order to remove emission lines from the model) to estimate the continuum in both the *Chandra* HETG nuclear and ACIS-S host spectra, and then model the remaining lines with Gaussians as before in §4.1. The line fluxes from the nuclear and host spectra are shown in Table 4 alongside the total line fluxes measured from the pn spectra. Reassuringly, the sum of the nuclear plus host are consistent with the total line fluxes, at least when we factor in statistical errors and cross-calibration differences.

After we account for contributions from the extended wings of the PSF using simulations from the MARX³⁸ ray-trace simulator (v4.5; Wise et al. 1997), we find that the extended Fe K α emission beyond $2''$ (>140 pc) comprises $28_{-8}^{+8}\%$ of the total. If the torus size is of order ≈ 4 – 10 pc, then we should probably consider the extended fraction above to be a lower limit to the cold reflection contribution from extended (i.e., non-torus) clouds, since there are likely to be contributions from similar material at 10–140 pc. Making a similar calculation for the ionized Fe He-like line, we find an extended fraction of $24_{-20}^{+18}\%$.

4.2.4. Combined Fit

We now combine the models of the nucleus and host galaxy from the *Chandra* spectra to fit the total spectra from *NuSTAR*, *XMM-Newton*, and *Swift* BAT. As highlighted previously, the emission below ≈ 2 keV is dominated by the numerous line and bremsstrahlung components, and thus does not provide much constraint on the properties of the reflectors. At the same time it contributes substantially to χ^2 , so for the remainder of the modeling we only consider the data above 2

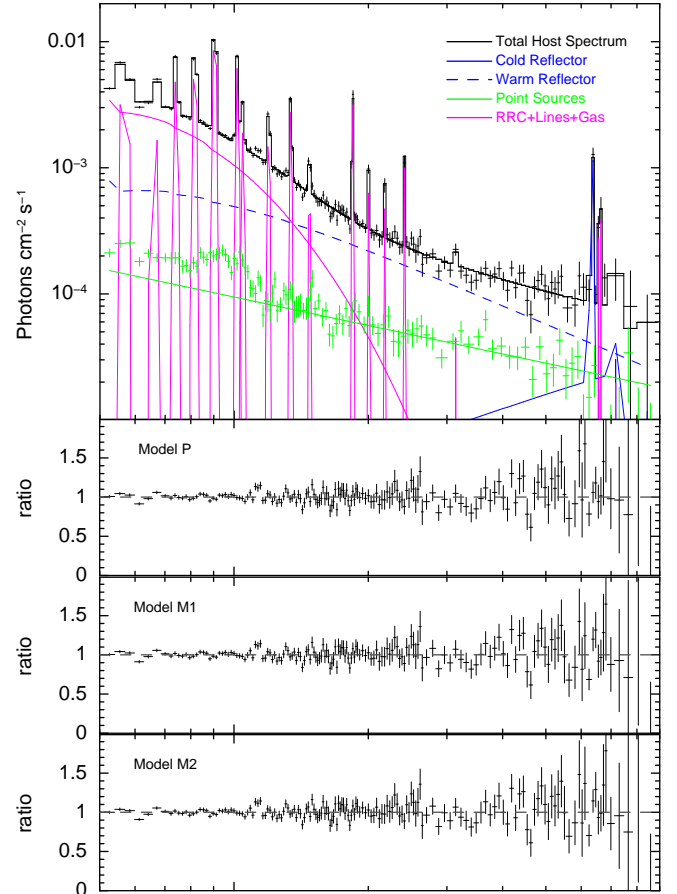


FIG. 7.— The total ACIS-S “host” unfolded spectrum (black) of all extranuclear emission extracted from a 2 – $75''$ annulus centered on the nucleus of NGC 1068. The host spectrum is fitted with four models comprised of partially absorbed cold and warm reflectors (blue solid and dashed lines, respectively), as well as RRC and the most prominent line components as identified by K14 (magenta solid lines), and the composite contribution from extranuclear point sources (green solid line). The top panel shows the fit to model P while the rest of the panels show the data-to-model ratios for models P, M1, and M2 respectively. The top panel also shows the composite ACIS-S extranuclear point-source spectrum (green), which is modeled above 1.5 keV as a $\Gamma_{\text{ULX}} = 1.2$ power law with a $E_c = 7$ keV exponential cutoff rollover.

keV. All of the spectral components that are well-constrained by the previous nuclear and host spectral fitting, such as the extranuclear point-source, RRC and line emission, are fixed, as we are primarily concerned with constraining the relative contributions from the warm and cold reflection, as well as any potential direct AGN continuum. For modeling simplicity, we also chose to ignore the regions between 2.3–2.5 keV and 6.5–6.8 keV, which correspond to regions of ionized Si and Fe line emission, respectively; these regions always have considerable residuals which are not modeled by the continuum reflection components but bias the component normalizations during the fitting process. We assume below that all of the components share a single intrinsic powerlaw slope and that any transmitted component, if present, must arise only from the nuclear portion of the spectrum. For selected relevant models below, we list the best-fit parameter values in Table 3 (“Total”) and/or plot their residuals in Figures 8–11.

Model P— We begin by fitting model P to the combined 2–195 keV spectra of NGC 1068. We fit Γ and Z_{Fe} , as well as

³⁸ <http://space.mit.edu/cxc/marx/>

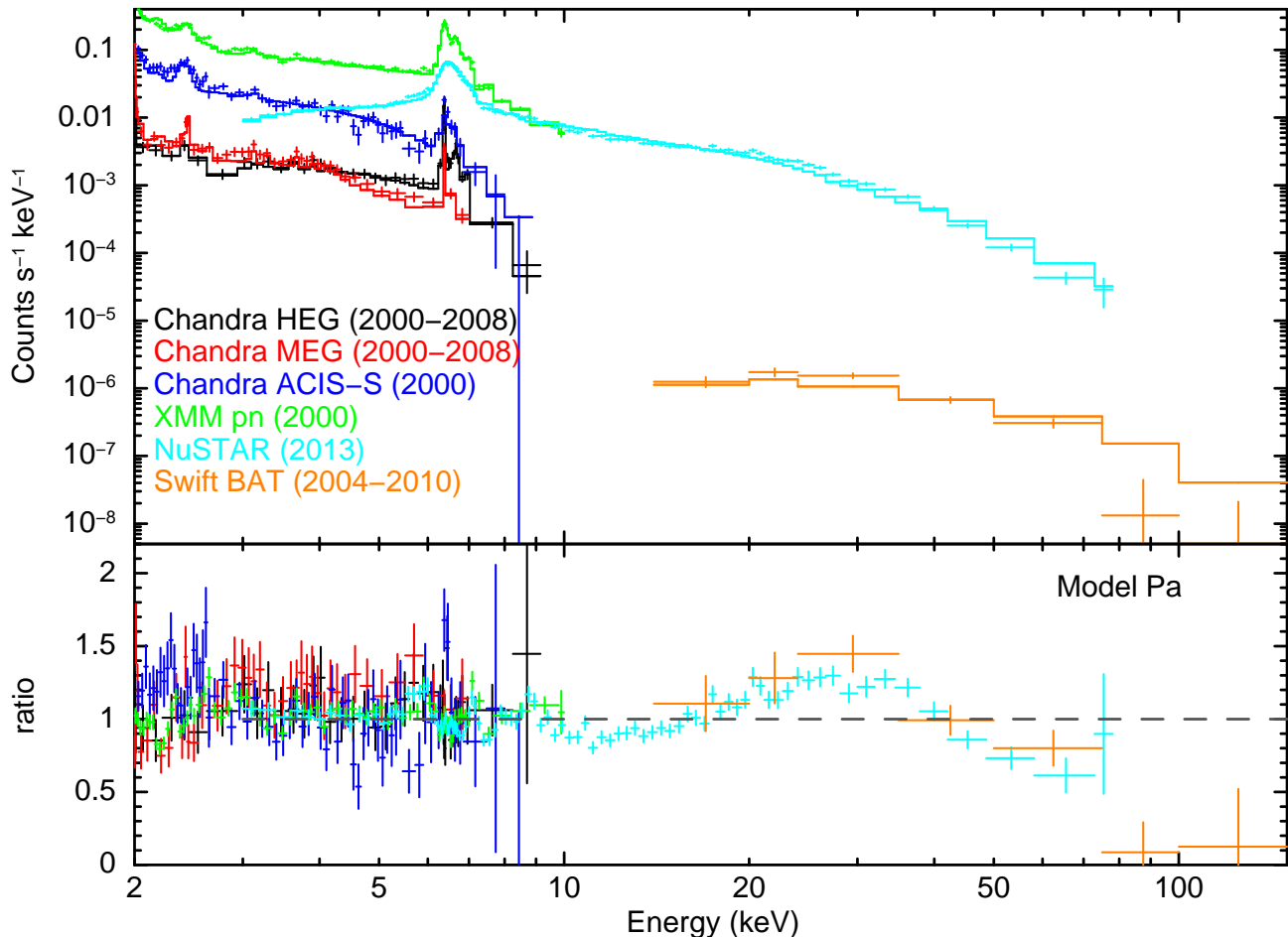


FIG. 8.— The top panel shows the final selection of X-ray spectra for NGC 1068 that we fitted from *NuSTAR* FPMA/FPMB (cyan), *XMM-Newton* pn (green), *Chandra* HEG/MEG (black/red), *Chandra* ACIS-S (blue), and *Swift* BAT (orange), all modeled with the best-fit parameters from model Pa, while the bottom panel shows the data-to-model ratios for each spectrum. As in Figure 2, the overall consistency between the various datasets is good, once known normalization offsets are accounted for. In particular, the sum of the *Chandra* HEG/MEG (“Nucleus only”) and ACIS-S (“Host only”) models provides an excellent fit to the other (“Total”) datasets where they overlap in energy. The only discrepancy between datasets appears to be a broad deficiency between 5.5–6.1 keV for the *NuSTAR* data. Model Pa is similar in shape to the M04a model, which still provides a poor fit to the data near the rise and peak of the Compton reflection hump. The HETG spectra are rebinned for presentation purposes.

the normalizations $A_{\text{cold,nuc}}$, $A_{\text{cold,host}}$, $A_{\text{warm,nuc}}$ and $A_{\text{warm,host}}$ as free parameters, while we fix $\theta_{\text{inc}} = 85^\circ$, $E_c = 500$ keV and $N_{\text{H}} = 10^{25}$ cm $^{-2}$. This model, hereafter “Pa”, yielded a poor fit, with a reduced $\chi^2_\nu = 1.34$ for $\nu = 1666$. The Pa model residuals, which are shown in Figure 8, highlight a general problem with fitting the spectral shape above 8 keV that we encountered with many of the adopted models, namely that the models either fit the spatially resolved < 10 keV data well but present clear > 10 keV residuals, or vice versa. Allowing the cutoff energy to vary failed to yield any improvement in χ^2_ν , with a best-fit value of $E_c = 500_{-176}^{\text{keV}}$, hereafter model “Pb”. Alternatively, allowing the inclination angle to also vary to $\theta_{\text{inc}} = 24_{-5}^{+7}$ deg, hereafter model “Pc”, significantly improved the fit, with a new reduced $\chi^2_\nu = 1.28$. We note that this inclination angle suggests a face-on configuration, perhaps indicative of scattering off of the back wall of a fiducial torus, while the best-fit photon index ($\Gamma = 1.65 \pm 0.02$) is somewhat lower than one would expect for such a high accretion rate source like NGC 1068 (e.g., $\Gamma = 2.5$; Fanali et al. 2013). Critically, although the high-energy residuals have improved, significant deviations of the form shown in Figure 8 from the observed continuum shape still remain. Again, vary-

ing the cutoff energy to $E_c = 387_{-176}^{\text{keV}}$ fails to yield any substantial improvement in χ^2_ν .

Model M1 — We now turn to the cold reflection as modeled by *MYTORUS*. As before, we initially adopt a “standard” fully coupled, uniform torus geometry, hereafter “M1a”. While there is no physical reason for the nuclear and extended components to be the same, we begin with such a scenario because it represents how previous studies would model the entire *XMM-Newton* or *NuSTAR* spectrum. For the M1a model, we fit $\Gamma = 1.40_{-0.09}^{\text{keV}}$ and the component normalizations, and fix the other parameters to $N_{\text{H}} = 10^{25}$ cm $^{-2}$, $\theta_{\text{inc}} = 90^\circ$, $E_{\text{cut}} = 500$ keV, and the S/L ratio to 1. Aside from allowing the reflection component normalizations to vary, the properties of the nucleus and host reflectors were tied together. The resulting fit was poor, with $\chi^2_\nu = 3.78$ for $\nu = 1666$, and large residuals around both the neutral Fe K α line and to a lesser extent the Compton hump. Moreover, the powerlaw slope is quite flat. From the residuals, it is clear that a S/L ratio of 1 is insufficient, and allowing the S/L ratio to vary to $26.7_{-1.0}^{+14.2}$, hereafter “M1b”, substantially improved the fit with $\chi^2_\nu = 1.78$. Such a S/L ratio is unreasonably high, however, and implies

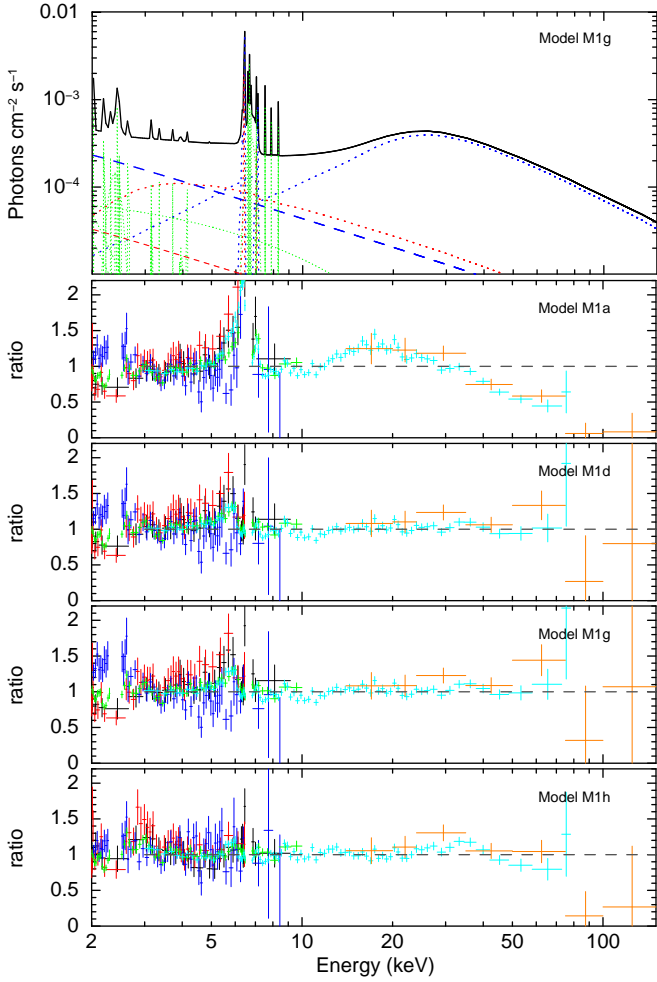


FIG. 9.— *Top panel:* Model M1g shown for the full dataset. Solid lines denote the overall spectrum. Blue lines represent the nuclear warm (dashed) and cold (dotted) reflection components. The red lines represent the host warm (dashed) and cold (dotted) reflection components. The RRC and line emission components for both the nuclear and host models are shown as dotted green lines. *Bottom panels:* Data-to-model ratios for several M1 models, with the same color-coding as Figure 8. Many of the models we fit exhibited poor fits to the data either above or below 10 keV. The HETG spectra are rebinned for presentation purposes.

that the adopted values for some of the fixed parameters are likely wrong. Varying E_{cut} to 55_{-5}^{+4} keV (“M1c”) lowered the S/L ratio to $15.0_{-0.9}^{+1.2}$ and resulted in $\chi^2_{\nu} = 1.61$. Finally, further varying the inclination angle and column density improves the fit to $\chi^2_{\nu} = 1.31$, with $\Gamma = 1.40_{-0.12}^{+0.12}$, $N_{\text{H}} = (9.4_{-3.3}^{+}) \times 10^{24} \text{ cm}^{-2}$, $\theta_{\text{inc}} = 78_{-4}^{+3}$, $E_{\text{cut}} = 41_{-4}^{+5}$ keV, and an S/L_{nuc+host} ratio of $3.8_{-0.8}^{+0.5}$ (“M1d”). This last model fits the >10 keV continuum significantly better, but at the expense of producing residuals in the <10 keV continuum (see Figure 9) while retaining a flat power-law slope. Ultimately, we conclude that none of the coupled MYTORUS models provides a reasonable fit to the continuum shape. It is important to point out that if we had only modeled either the <10 keV spectra or the total aperture spectra, we would have arrived at a satisfactory χ^2_{ν} .

As an alternative to the fully coupled models, we tried fitting separate MYTS+MYTL parameters for the nucleus and the host spectra, as might be expected for the combination of a thick torus and more tenuously distributed larger scale molecular clouds, which has been found from mid-IR con-

straints on NGC 1068. We began by fitting a single photon index $\Gamma = 1.80_{-0.07}^{+0.05}$, the various component normalizations, and independent column densities $N_{\text{H,nuc}} = (9.8_{-0.2}^{+}) \times 10^{24} \text{ cm}^{-2}$ and $N_{\text{H,host}} = (2.4_{-0.2}^{+0.1}) \times 10^{23} \text{ cm}^{-2}$ and S/L ratios $12.2_{-1.9}^{+1.8}$ and $0.5_{-0.2}^{+0.3}$ for the nucleus and host components, respectively, while fixing $\theta_{\text{inc}} = 90^\circ$ and $E_{\text{cut}} = 500$ keV (“M1e”). This fit produced a reduced $\chi^2_{\nu} = 1.54$ for $\nu = 1663$. Allowing $E_{\text{cut}} = 33_{-3}^{+5}$ keV improved the fit to $\chi^2_{\nu} = 1.30$, with modest changes to the other free parameters such that the Γ remained pinned at its minimum while $N_{\text{H,nuc}} = (5.3_{-0.5}^{+0.4}) \times 10^{24} \text{ cm}^{-2}$, $N_{\text{H,host}} = (0.09 \pm 0.03) \times 10^{24} \text{ cm}^{-2}$, $S/L_{\text{nuc}} = 10.8_{-0.8}^{+1.3}$ and $_{\text{host}} = 1.0_{-0.2}^{+0.4}$ (“M1f”). Finally, allowing the inclination angles to vary (“M1g”) only marginally improves the fit to $\chi^2_{\nu} = 1.28$, with free parameters $\Gamma = 1.40_{-0.34}^{+0.34}$, $E_{\text{cut}} = 34_{-4}^{+58}$ keV, $N_{\text{H,nuc}} = (8.0_{-1.6}^{+}) \times 10^{24} \text{ cm}^{-2}$, $N_{\text{H,host}} = (1.3_{-0.9}^{+1.5}) \times 10^{24} \text{ cm}^{-2}$, $S/L_{\text{nuc}} = 3.5_{-0.5}^{+0.8}$ and $S/L_{\text{host}} = 1.5 \pm 0.3$.

We note that freeing the column density and normalization toward the transmitted component (“M1h”) to $N_{\text{H,trans}} = (6.0_{-0.8}^{+1.3}) \times 10^{24} \text{ cm}^{-2}$ results in a reduced $\chi^2_{\nu} = 1.13$, with best-fit values of $\Gamma = 2.20_{-0.12}^{+0.07}$, $E_{\text{cut}} = 72_{-21}^{+75}$ keV, $N_{\text{H,nuc}} = (2.6_{-0.5}^{+0.5}) \times 10^{23} \text{ cm}^{-2}$ and $N_{\text{H,host}} = 10^{25} \text{ cm}^{-2}$ (unconstrained), $S/L_{\text{nuc}} = 1.0_{-0.3}^{+0.2}$ and $S/L_{\text{host}} = 2.0_{-0.6}^{+0.6}$, and inclination angles of $0.7_{-4.5}^{+4.5}$ deg and $1.9_{-10.5}^{+10.5}$ deg for the nucleus and host components, respectively. This model is the best version of the “standard” MYTORUS configuration and crudely models the key continuum and line features, but ultimately predicts that NGC 1068 should be dominated by the transmitted component above 20 keV. The normalizations of the various continuum components are $A_{\text{trans}} = 2.6_{-1.3}^{+1.3}$ photons keV⁻¹ cm⁻² s⁻¹ at 1 keV, $A_{\text{warm,nuc}} = (3.0_{-1.3}^{+1.3}) \times 10^{-4}$ photons keV⁻¹ cm⁻² s⁻¹ at 1 keV, $A_{\text{cold,nuc}} = (4.0_{-0.5}^{+0.7}) \times 10^{-2}$ photons keV⁻¹ cm⁻² s⁻¹ at 1 keV, $A_{\text{warm,host}} = (3.9_{-1.4}^{+1.5}) \times 10^{-4}$ photons keV⁻¹ cm⁻² s⁻¹ at 1 keV, $A_{\text{cold,host}} = (9.4_{-3.7}^{+4.2}) \times 10^{-3}$ photons keV⁻¹ cm⁻² s⁻¹ at 1 keV, respectively, implying a covering fractions of ~ 0.008 and ~ 0.002 for the nucleus and host cold reflection components. Such low covering fractions run contrary to the variability constraints presented in §2.1 and §2.6. As such, the good fit appears to be a consequence of allowing freedom for several spectral components to fit small portions of the overall spectrum, and is presumably degenerate in this sense.

We conclude that the “standard” configuration of MYTORUS has considerable difficulty reproducing the main spectral and temporal X-ray characteristics of NGC 1068.

Model M2— We now turn to the second MYTORUS configuration, which employs two MYTORUS Compton scatterers fixed at 0° and 90° , representing a potential clumpy torus-like distribution. Following the discussion in §4.2.2, we only invoke the 0° component to fit the host spectrum. We began by fitting a basic form of this model, hereafter “M2a”, with varying $\Gamma = 2.29_{-0.02}^{+0.04}$ and component normalizations with the remaining parameters fixed to $N_{\text{H}} = 10^{25} \text{ cm}^{-2}$, $S/L_{\text{nuc+host}} = 1.0$, and $E_{\text{cut}} = 500$ keV for all scattering components. The best fit returns a $\chi^2_{\nu} = 1.84$ for $\nu = 1666$, which is a significant improvement over model M1a. However, the continuum is still not well-fit and the best-fit $A_{\text{nuc,MYTS},90}$ normalization is consistent with zero ($<1\%$ of cold reflector flux). Fitting the S/L_{nuc+host} ratio to $4.3_{-0.3}^{+0.4}$ (“M2b”) reduces $\chi^2_{\nu} = 1.51$, and yields $\Gamma = 1.49 \pm 0.04$ plus moderate variations in the component normalizations. M2b offers a significant improvement

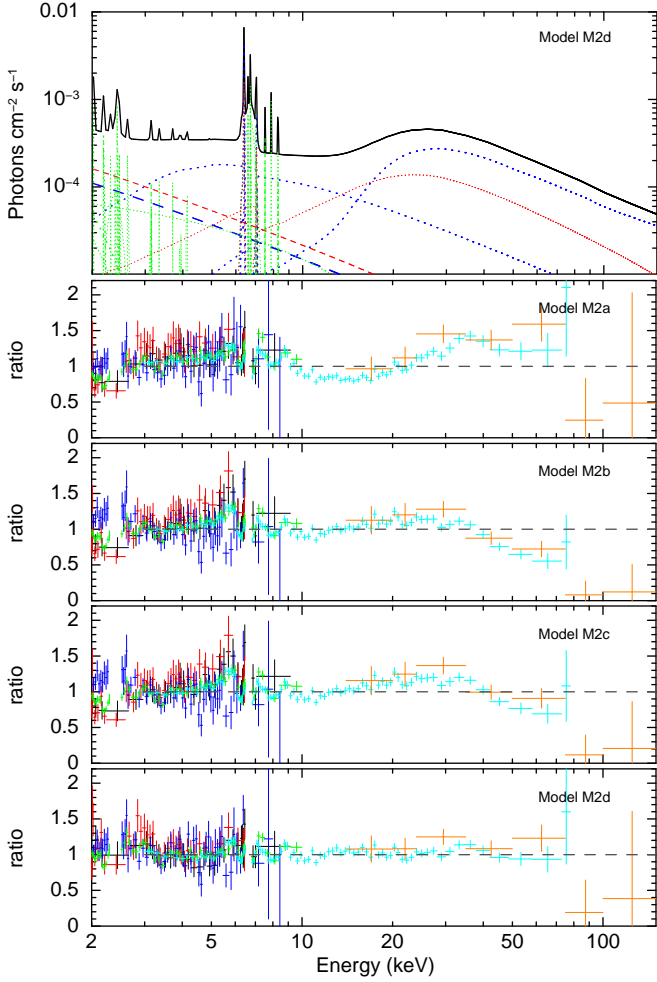


FIG. 10.— Same as Figure 9, but for M2 models. The model M2d provides the best overall fit to the spectra among all of the models.

over model M1b. Additionally varying $E_{\text{cut}} = 146^{+76}_{-50}$ keV (“M2c”), provides only very marginal improvement ($\chi^2_{\nu} = 1.48$) and leaves the parameters largely unmodified. Finally, varying the three column densities (“M2d”) improves the fit to $\chi^2_{\nu} = 1.14$, with $\Gamma = 2.10^{+0.06}_{-0.07}$, a $S/L_{\text{nuc+host}}$ ratio of 1.0 ± 0.1 , $E_{\text{cut}} = 128^{+115}_{-44}$ keV $N_{\text{H,nuc},90} = (10.0^{+0.5}_{-4.4}) \times 10^{24}$ cm $^{-2}$, $N_{\text{H,nuc},0} = (1.5 \pm 0.1) \times 10^{23}$ cm $^{-2}$, $N_{\text{H,host},0} = (5.0^{+4.5}_{-1.9}) \times 10^{24}$ cm $^{-2}$, and normalizations of $A_{\text{warm,nuc}} = (2.5^{+0.3}_{-0.4}) \times 10^{-4}$ photons keV $^{-1}$ cm $^{-2}$ s $^{-1}$ at 1 keV, $A_{\text{cold,nuc},90} = (3.0 \pm 0.5) \times 10^{-1}$ photons keV $^{-1}$ cm $^{-2}$ s $^{-1}$ at 1 keV, $A_{\text{cold,nuc},0} = (3.6^{+0.3}_{-0.2}) \times 10^{-2}$ photons keV $^{-1}$ cm $^{-2}$ s $^{-1}$ at 1 keV, $A_{\text{warm,host}} = (3.4^{+0.3}_{-0.4}) \times 10^{-4}$ photons keV $^{-1}$ cm $^{-2}$ s $^{-1}$ at 1 keV, $A_{\text{cold,host},0} = (1.0 \pm 0.2) \times 10^{-2}$ photons keV $^{-1}$ cm $^{-2}$ s $^{-1}$ at 1 keV. Freezing the high-energy cutoff at $E_{\text{cut}} = 500$ keV (“M2e”) leaves the above parameters virtually unchanged and $\chi^2_{\nu} = 1.16$.

As can be seen in Figure 10, the data-to-model ratio residuals are now fairly flat out to ≈ 80 keV. The primary difference between model M2d (or M2e) and all of the others lies in how the nuclear $\theta_{\text{inc}} = 0^\circ$ cold reflector component, due to its significantly lower N_{H} , is able to fill in the spectral gap around 4–8 keV between the “normal” cold and warm reflectors. One important aspect of this model which deserves highlighting is the fact that while the higher N_{H} component provides the bulk

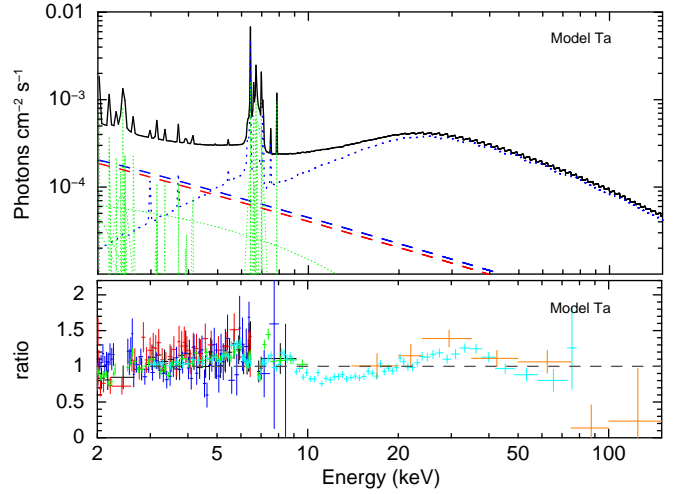


FIG. 11.— Same as Figure 9, but for T models.

of the flux to the Compton hump, it does not contribute much to the Fe fluorescence line emission. Instead, the lower N_{H} component produces the bulk of the Fe fluorescence line emission and dominates the continuum peaking around 5–10 keV. Thus the two key features of Compton reflection, namely the hump and Fe line, need not arise from a single absorber and in fact likely arise from different obscuring clouds. Assuming a single absorber will likely lead to misinterpretations.

Model T— Finally, we fit the cold reflection with the torus model. As noted in §4.2, this model is not suitable for fitting the host spectrum, so we instead modeled the host spectrum identically to the M2 case using MYTS+MYTL components with an inclination of $\theta_{\text{inc}} = 0^\circ$. Varying $\Gamma = 1.96^{+0.05}_{-0.04}$, $\theta_{\text{open}} = 64^{+3}_{-2}$ deg, and component normalizations, with fixed values of $N_{\text{H}} = 10^{25}$ cm $^{-2}$, $\theta_{\text{inc}} = 87^\circ$, $E_{\text{cut}} = 500$ keV, and a S/L_{host} ratio of 1.0, yielded a reduced $\chi^2_{\nu} = 1.61$ for $\nu = 1666$ (“Ta”). This provides a relatively poor fit, with residuals near the Fe lines and >10 keV continuum (Figure 11). Freeing the torus inclination angle to $\theta_{\text{T,inc}} = 87^{+16}_{-16}$ (“Tb”) does not improve the fit. Further varying the nuclear and host column densities to $N_{\text{H,nuc}} = (6.9^{+0.6}_{-0.8}) \times 10^{24}$ cm $^{-2}$, $N_{\text{H,host},0} = (10.0^{+0.6}_{-6.6}) \times 10^{24}$ cm $^{-2}$ (“Tc”) leads to a modest improvement $\chi^2_{\nu} = 1.57$, with $\Gamma = 2.13^{+0.04}_{-0.06}$, $\theta_{\text{open}} = 69^{+4}_{-3}$ deg, and $\theta_{\text{incl}} = 87^{+12}_{-12}$ deg. As with other models, there are significant residuals as the model fails to fit the continuum shape well. In all cases, the host cold reflection normalization is consistent with zero. It seems that the torus model does not provide enough flexibility to model the transmission and scattered components separately and again we conclude that the torus model has considerable difficulty reproducing the main spectral X-ray characteristics of NGC 1068.

4.2.5. Model Summary

We tested a variety of cold reflection models earlier in this section. As has been traditionally done in the past, we modeled NGC 1068 with a single monolithic cold reflector using *pexmon* (models Pa–Pc), *MYTorus* (models M1a–M1d), and *torus* (models Ta–Tc). Alternatively, we also modeled NGC 1068 with multiple reflectors using two or three *MYTorus* components to fit the two spatially distinct nuclear and host regions (models M1e–M1h) and additional complexity in the nuclear spectrum (models M2a–M2d). We found

that many models are able to fit either the spatially resolved < 10 keV spectra or the total aperture spectra well, but generally not both.

The two models which do manage to fit all of the spectra well are M1h and M2d. In both cases, a cold reflection component with $N_{\text{H}} \sim 10^{23}$ cm $^{-2}$ peaking at 5–10 keV is required to fill in a critical gap in the model where the declining warm reflector and the increasing cold reflector meet. Model M1h is rejected, however, because it requires a strong transmitted component, which runs contrary to our variability results (§3), leaving only M2d as our preferred model.

When modeling M2d, we find a best-fit power-law slope of $\Gamma = 2.10^{+0.06}_{-0.07}$, which is marginally higher than the average AGN value of $\Gamma \sim 1.9$ (e.g., Reeves & Turner 2000). Notably, high Γ values are often associated with high Eddington ratio systems (e.g., Shemmer et al. 2006; Risaliti et al. 2009; Brightman et al. 2013), and thus the slope here is consistent with our initial accretion rate assessment in §1. The high-energy cutoff value for this model, $E_{\text{cut}} = 128^{+115}_{-44}$ keV is perhaps somewhat low. This could imply low coronal temperatures, although the error bars indicate this value is not well constrained. With this model, we derive total observed X-ray luminosities of $L_{2-10\text{keV,obs}} = 1.8 \times 10^{41}$ erg s $^{-1}$ and $L_{10-40\text{keV,obs}} = 5.6 \times 10^{41}$ erg s $^{-1}$, and intrinsic³⁹ X-ray luminosities of $L_{2-10\text{keV,intr}} = 2.2 \times 10^{43}$ erg s $^{-1}$ and $L_{10-40\text{keV,intr}} = 1.5 \times 10^{43}$ erg s $^{-1}$, respectively. This intrinsic $L_{2-10\text{keV}}$ value is only a factor of ≈ 1.6 lower than that predicted by mid-IR to X-ray relation of Gandhi et al. (2009), despite the obvious spectral complexity that we find.

We stress that the scattered emission from NGC 1068 is clearly complex and thus the models attempted were by no means exhaustive. Alternative complex component combinations likely exist which can fit the obvious Compton hump and Fe fluorescence line as well as strike a balance in the overall reflection continuum levels. Nonetheless, we can conclude that simple configurations such as a single nuclear reflector or a patchy torus fail to match the data, and an additional lower column density component is needed.

5. DISCUSSION

From the combined modeling we performed in the previous section, there are a few points worth stressing.

The quality of the *NuSTAR* data plays an important role in constraining the fits. With poorer quality data, such as that from *Suzaku*, *BeppoSAX*, or *Swift* BAT shown in Figure 2, several of the models we considered produce acceptable fits. Only with the *NuSTAR* data can we observe in detail the nature of the rising Compton hump and broad peak, which is difficult to fit with a single cold reflection model. Likewise, fitting the *Chandra* nuclear and host spectra separately, we find that the combination of good-quality nuclear and host spectra creates considerable tension for several models which would otherwise fit the total *XMM-Newton* and *NuSTAR* spectra at acceptable levels. This study demonstrates that it can be important to have both high-quality spectra above 10 keV and spatially resolved X-ray spectra in order to, e.g., reject simple monolithic cold reflection models. The recent analysis of the Circinus Galaxy by Arévalo et al. (2014) also benefited from the powerful combination of high-quality *NuSTAR* data and spatial separation of the nuclear and host components, demonstrating that there too a significant fraction of the warm and

cold reflection components arise from well beyond $2''$ (i.e., 38 pc at the distance of Circinus).

These two objects are among the closest and X-ray brightest Compton-thick AGN on the sky, and benefit from a wealth of high-quality X-ray data. Unfortunately, there are only a handful of nearby Compton-thick AGN where a similar analysis can be made, but it will be interesting to see how diverse parameter space might be with respect to this multiple cold reflector model. For fainter and more distant obscured X-ray AGN, however, we can only obtain modest-to-poor quality *NuSTAR* data. Moreover, with the angular resolution of currently available instruments, we will be unable to separate the 2–8 keV nuclear emission from its host. So while it may be possible to model the total emission from such AGN in reasonable detail and with acceptable results (e.g., Baloković et al. 2014; Gandhi et al. 2014; Lansbury et al. 2014; Del Moro et al. 2014, Brightman et al. 2015 in prep), it will not be possible to investigate the detailed physical properties of such sources, as for NGC 1068 and Circinus (Arévalo et al. 2014). The work here and in Circinus highlight the potential issues of modeling a total spectrum from, e.g., *XMM-Newton* or *NuSTAR* with a monolithic model of the obscurer. For the multiple cold reflector model shown in Figure 10, different portions of the total reflection spectrum seen by *NuSTAR* and *XMM-Newton* appear to arise from different obscuring clouds, decoupling the two key features of cold reflection. The fact that cold reflectors occur on a variety of physical scales or with a variety of column densities is unlikely to change the basic requirement for a high column density associated with a mildly or heavily Compton-thick AGN. However, it is possible for this variety to change interpretations regarding the relative Fe abundance, inclination angle, covering factor for a given column density, and high-energy cutoff; we observed several of these to vary significantly from model to model in §4.2.

Although unobscured AGN are dominated by the transmitted power law, the Fe line and Compton hump do imprint themselves as secondary contributions. To test how our preferred model of NGC 1068 might affect the fitting of unobscured AGN, we inverted the inclination angles of the MYTORUS components by 90° and added a relativistically blurred ionized disk reflection component (`relconv*xillver`; Dauser et al. 2013; García et al. 2014). We linked the disk reflection parameters to previously determined values (e.g., Γ , E_{cut} , θ_{inc} , Z_{Fe}), or fixed them to their default values. We normalized the disk reflection relative to the other components such that it provides the same contribution at 30 keV as the combined cold reflection components. In this configuration, the relative total reflection flux is high, comprising $\approx 30\%$ of the total at 30 keV, yet the narrow observed Fe $K\alpha$ equivalent width (EW) is only 40 eV; the latter value is toward the low end of EW measurements made for Seyfert 1s (e.g., Yaqoob & Padmanabhan 2004) and implies that the narrow Fe $K\alpha$ EW may not be a useful estimator for the relative strength of the cold reflection component, as is sometimes assumed, and even low EW Fe lines may signify important scattered-light contributions at higher energies.

We then varied the exponential cutoff energy for our unobscured version of NGC 1068 between three values (100, 300, and 500 keV). We simulated a 50 ks *NuSTAR* spectrum, resulting in $\sim 10^6$ 3–79 keV photons, and fit this with a model typical of those used in unobscured AGN studies (i.e., where the transmitted, disk reflection, and cold reflection are modeled as

³⁹ This does not include contributions from scattered components or contamination.

(cutoffpl+relcov*xillver+pexrav+zgauss, respectively, absorbed by a low column density t_{babsGal}). We allowed Γ , E_{cut} , Z_{Fe} , and the component normalizations to vary, and fixed the remaining parameters at typical values (e.g., $Xi = 3.1$, $Z_{\text{Fe}} = 3$, $a = 0.9$, $\cos\theta_{\text{pexrav}} = 0.3$, $\theta_{\text{xillver}} = 20^\circ$). In all cases, we obtained reasonable fits with $\chi_\nu \approx 1.0$ – 1.1 and found that the powerlaw slope was consistent with its input value. For input E_{cut} values of 100, 300, and 500 keV, we obtained best-fit values of 312_{-32}^{+43} , 227_{-16}^{+27} , 302_{-30}^{+37} keV, respectively, and $Z_{\text{Fe}} = (0.7\text{--}0.8) \pm 0.1$. We ran another simulation, naively assuming the M2d reflection components were globally the same, which yielded similar results for the cutoff energies. Such toy models are admittedly far from conclusive due to the likely large number of permutations of possible spectral shapes of components and degeneracies among parameters, not to mention the manner in which we implemented the high-energy cutoff for MYTORUS. Nonetheless, they do highlight how errors on some quantities such as the high-energy cutoff could be underestimated even in unobscured AGN and can strongly depend on what model assumptions are adopted.

The best-fit model for the composite X-ray dataset, M2d, could be visualized as follows. In the inner $2''$ (140 pc) region, we see a $\theta_{\text{inc}} = 90^\circ$ (fixed), $N_{\text{H}} \approx 10^{25} \text{ cm}^{-2}$ reflector with a covering factor of 0.5 (fixed), which to first order is presumably associated with a standard, compact, torus-like structure. Additionally, we find a $\theta_{\text{inc}} = 0^\circ$ (fixed), $N_{\text{H}} \approx 10^{23} \text{ cm}^{-2}$ reflector with an estimated covering factor of 0.13, based on the relative component normalizations, which appears to act as a screen. This less dense component could be more or less co-spatial with the dense torus or it could be material in the ionization cone. In both cases, we might expect a stratification of dense material stemming from instabilities associated with the photoionization of the dense molecular gas by AGN radiation field structures (e.g., akin to the structures at the boundaries between HII regions and molecular clouds; e.g., Pound 1998). Or alternatively, it could simply be reflection from larger-scale interstellar clouds aggregating within the inner ≈ 100 pc (e.g., Molinari et al. 2011). In all cases, we should expect a range of clouds which follow a log-normal column density distribution (e.g., Lada et al. 1999; Goodman et al. 2009; Lombardi et al. 2010; Tremblin et al. 2014). This should in turn introduce considerable complexity into the AGN reflection components. We appear to be seeing the first hints of this anticipated complexity in NGC 1068. We note that this less dense reflection component produces the bulk of the Fe K α line emission and, moreover, we see no strong long-term variability from the < 10 keV continuum or line flux. Thus we conclude that this second reflection component likely arises light years from the central AGN and/or is distributed enough to wash out any variability.

We note that at a basic level, the above multi-component reflector configuration found in the nuclear region appears reasonably consistent with the picture stemming from mid-IR interferometry for NGC 1068 (e.g., Jaffe et al. 2004; López-Gonzaga et al. 2014), whereby a three-component model, comprised of a small obscuring torus and two dusty structures at larger scales (at least 5–10 pc), best fits the data. The larger scale dust is off-center and could represent the inner wall of a dusty cone (e.g., the ionization cone). Based on the compactness and detailed modeling of spectral energy distributions in various AGN, these structures are believed to be clumpy and comprised of a range of torus clouds with column densities of $N_{\text{H}} \sim 10^{22}$ – 10^{23} cm^{-2} (e.g., Elitzur & Shlosman

2006; Nenkova et al. 2008; Ramos Almeida et al. 2009).

On more extended ($> 2''$) scales, we find an additional $\theta_{\text{inc}} = 0^\circ$ (fixed), $N_{\text{H}} \approx (4\text{--}10) \times 10^{24} \text{ cm}^{-2}$ reflector with a covering factor of 0.03. The inclination angle, if left free, is not strongly constrained, and thus it is not clear whether this component is a screen, a mirror, or perhaps both. This material could be associated with clumpy molecular clouds either within the ionization cone or the general interstellar cloud population in the host galaxy. Intriguingly, our separation of nuclear and host spectra was purely based on instrumental reasons, and thus, if the distribution of clouds is strongly centralized and goes roughly as $1/r$ or $1/r^2$ (e.g., Bally et al. 1988; Nenkova et al. 2008), then we might expect at least a fraction of the Fe K α line flux currently assigned to the $N_{\text{H}} \approx 10^{25} \text{ cm}^{-2}$ torus-like nuclear reflection component to in fact arise from reflection by extended material. This suggests that a non-negligible portion of the overall reflection component in NGC 1068 arises outside of the torus. As we found in §4.2.3, the empirical fraction of extended Fe K α flux is substantially higher ($\approx 30\%$) than the estimate of the overall reflection, suggesting that perhaps there are multiple N_{H} components responsible for the extended emission as well. Based on the same molecular cloud distribution argument as above, it may be possible for the majority of the narrow Fe K α emission to originate from radii well beyond the classic torus.

6. CONCLUSIONS

We have characterized the X-ray spectra of the archetypal Compton-thick AGN, NGC 1068, using newly acquired *NuSTAR* data, combined with archival data from *Chandra*, *XMM-Newton*, and *Swift* BAT. We modeled NGC 1068 with a combination of a heavily obscured transmitted power law, scattering by both warm and cold reflectors, radiative recombination continuum and line emission, and off-nuclear point source emission, employing a handful of cold reflector models. Our primary results can be summarized as follows:

- The > 10 keV *NuSTAR* data are consistent with past measurements to within cross-calibration uncertainties, but provide at least an order of magnitude more sensitivity, allowing us to constrain the high-energy spectral shape of NGC 1068 in better detail than ever before. We find no strong evidence for short- or long-term variability, consistent with the primary transmitted continuum being completely obscured from our line-of-sight.
- We use *Chandra* ACIS-S and HETG data to split the reflection-dominated spectrum of NGC 1068 into two spatial regimes representing the nuclear ($< 2''$) and host ($2\text{--}75''$) contributions to the total spectrum measured by *NuSTAR*, *XMM-Newton*, and *Swift* BAT. Because reflection arises from the two distinct spatial regimes, modeling both components together allow us to break previously unexplored degeneracies to aid physical interpretation.
- Modeling NGC 1068 as a monolithic cold reflector with a single column density N_{H} generally fails to reproduce some critical portion of the combined spectra accurately and/or yields parameters which are difficult to reconcile with robust independent observations, regardless of the Compton-reflection model used.
- Modeling NGC 1068 using a multi-component reflector (here as best-fit model M2d with two nuclear and one

extended MYTORUS components with best-fit values of $\Gamma \approx 2.1$, $E_{\text{cut}} \gtrsim 90$ keV, $N_{\text{H}} = 10^{25}$ cm $^{-2}$, $N_{\text{H}} \approx 1.5 \times 10^{23}$ cm $^{-2}$, and $N_{\text{H}} \approx 5 \times 10^{24}$ cm $^{-2}$, respectively, was able to reproduce all of the primary spectral lines and continuum shape around the Compton hump. In this best-fit multi-component reflector model, the higher N_{H} components contributed flux primarily to the Compton hump above 10 keV while the lower N_{H} nuclear reflector is needed to reproduce the curvature of the continuum around 10 keV and it also provides the missing Fe line flux to model the whole structure with solar (as opposed to highly supersolar) metallicity. Thus, this configuration effectively decouples the two key features of Compton reflection which are typically assumed to be coupled.

- There are strong differences in the ratios of the 2–10 keV fluxes of the warm and cold reflection components, depending on the model employed and the parameters being fit. Because of the decoupling mentioned above, it could be dangerous to extrapolate the full properties of the reflector using simple reflection models, as has typically been done in the past with either lower-quality data or in type 1 AGNs diluted by transmitted continuum. We note that this decoupling could be at least partially responsible for some of the apparently high Fe abundances which have been quoted in the literature (e.g., M04).
- Considering only the *Chandra* data, we find that $\approx 30\%$ of the neutral Fe $K\alpha$ line flux arises from $>2''$ (≈ 140 pc) in an extended configuration. Extrapolating this fraction inward assuming an increasing solid angle of dense molecular clouds implies that a significant fraction (and perhaps the majority) of the Fe $K\alpha$ line arises from Compton-scattering off of material well outside of the fiducial 1–10 pc torus material. A follow-up investigation looking into the spatial distribution of this material around several local AGN will be presented in Bauer et al. (2015, in preparation).
- The multi-component reflector configuration envisioned here comprises a compact Compton-thick torus-like structure covering 50% of the sky and more tenuous, extended $N_{\text{H}} \approx 10^{23}$ cm $^{-2}$ clouds covering $\approx 13\%$ of the sky within the nuclear region (<140 pc), as well as larger-scale, low-covering factor Compton-thick clouds which extend out to 100s of pc. This scenario bears striking similarities to the multiple dust structures found via mid-IR interferometry for NGC 1068, and may eventually allow some independent corroboration of the clumpy torus model.

The benefits of combining high-quality >10 keV spectral sensitivity from *NuSTAR* and spatially resolved spectroscopy from *Chandra* are clear, and could offer novel constraints on the few dozen closest, brightest AGN on the sky. Moving

on to fainter and more distant objects, however, is likely to be challenging with current instrumentation due to the extremely long integrations required and the increasingly poor intrinsic spatial resolutions obtained. Moreover, we should caution that our best-fit multi-component reflector, which we modeled only with three distinct column densities, could be an oversimplification, and in fact there might be a continuous distribution of different column-density reflectors, given that the Galactic molecular cloud probability distribution function is well represented by a power law over a wide range of column densities (e.g., Lada et al. 1999; Goodman et al. 2009; Lombardi et al. 2010). Each cloud might contribute something to the overall reflection spectrum, thereby modifying the spectral shape away from that of a single monolithic reflector. Hopefully by acquiring similar constraints in other nearby Compton-thick AGN to those found for NGC 1068 and Circinus, combined with an assessment of the parameter space for obscuring clouds from mid-IR interferometry studies, we can amass enough clues in the short term to model distant and/or faint objects in a more informed manner. Ultimately, if the *Athena* mission (Nandra et al. 2013; Nandra 2014) can achieve its best-case scenario for spatial resolution of a few arcseconds, it could open up spatially resolved Fe analysis to a significantly larger range of AGN and help us to place these local AGN in broader context.

This work was supported under NASA Contract No. NNG08FD60C, and made use of data from the *NuSTAR* mission, a project led by the California Institute of Technology, managed by the Jet Propulsion Laboratory, and funded by the National Aeronautics and Space Administration. We thank the *NuSTAR* Operations, Software and Calibration teams for support with the execution and analysis of these observations. This research has made use of the *NuSTAR* Data Analysis Software (NuSTARDAS) jointly developed by the ASI Science Data Center (ASDC, Italy) and the California Institute of Technology (USA). This research has made use of data obtained through the High Energy Astrophysics Science Archive Research Center (HEASARC) Online Service, provided by the NASA/Goddard Space Flight Center. We acknowledge financial support from the following: CONICYT-Chile Basal-CATA PFB-06/2007 (FEB, ET), FONDECYT grants 1141218 (FEB), 1140304 (PA), 1120061 (ET), and Anillo grant ACT1101 (FEB, PA, ET); Project IC120009 “Millennium Institute of Astrophysics (MAS)” funded by the Iniciativa Científica Milenio del Ministerio de Economía, Fomento y Turismo (FEB); Swiss National Science Foundation through the Ambizione fellowship grant PZ00P2_154799/1 (MK); *NuSTAR* subcontract 44A-1092750 (WNB, BL); NASA ADP grant NNX10AC99G (WNB, BL); ASI/INAF grant I/037/12/0-011/13 (SP, AC, AM and GM); and STFC grant ST/J003697/1 (PG).

Facilities: CXO (ACIS, HETG), XMM (pn, MOS), NuSTAR (FPMA, FPMB), Swift (XRT, BAT), BeppoSAX (MECS, PDS), Suzaku (XIS, PIN),

REFERENCES

- Alonso-Herrero, A., et al. 2011, *ApJ*, 736, 82
 Antonucci, R. 1993, *ARA&A*, 31, 473
 Antonucci, R. R. J. & Miller, J. S. 1985, *ApJ*, 297, 621
 Arévalo, P., Churazov, E., Zhuravleva, I., Hernández-Monteagudo, C., & Revnivtsev, M. 2012, *MNRAS*, 426, 1793
 Arévalo, P., et al. 2014, *ApJ*, 791, 81
 Bachetti, M., et al. 2013, *ApJ*, 778, 163
 Bally, J., Stark, A. A., Wilson, R. W., & Henkel, C. 1988, *ApJ*, 324, 223
 Baloković, M., et al. 2014, *ApJ*, 794, 111
 Baumgartner, W. H., Tueller, J., Markwardt, C. B., Skinner, G. K., Barthelmy, S., Mushotzky, R. F., Evans, P. A., & Gehrels, N. 2013, *ApJS*, 207, 19

- Bock, J. J., et al. 2000, *AJ*, 120, 2904
- Boldt, E. 1987, *Phys. Rep.*, 146, 215
- Brightman, M. & Nandra, K. 2011, *MNRAS*, 413, 1206
- Brightman, M., et al. 2013, *MNRAS*, 433, 2485
- Brinkman, A. C., Kaastra, J. S., van der Meer, R. L. J., Kinkhabwala, A., Behar, E., Kahn, S. M., Paerels, F. B. S., & Sako, M. 2002, *A&A*, 396, 761
- Canizares, C. R., et al. 2000, *ApJ*, 539, L41
- Capetti, A., Axon, D. J., & Macchetto, F. D. 1997, *ApJ*, 487, 560
- Cecil, G., Bland, J., & Tully, R. B. 1990, *ApJ*, 355, 70
- Cecil, G., Dopita, M. A., Groves, B., Wilson, A. S., Ferruit, P., Pécontal, E., & Binette, L. 2002, *ApJ*, 568, 627
- Crenshaw, D. M. & Kraemer, S. B. 2000, *ApJ*, 532, L101
- Dauser, T., García, J., Wilms, J., Böck, M., Brenneman, L. W., Falanga, M., Fukumura, K., & Reynolds, C. S. 2013, *MNRAS*, 430, 1694
- Del Moro, A., et al. 2014, *ApJ*, 786, 16
- Dopita, M. A., Groves, B. A., Sutherland, R. S., Binette, L., & Cecil, G. 2002, *ApJ*, 572, 753
- Elitzur, M. & Shlosman, I. 2006, *ApJ*, 648, L101
- Evans, I. N., Ford, H. C., Kinney, A. L., Antonucci, R. R. J., Armus, L., & Caganoff, S. 1991, *ApJ*, 369, L27
- Fabian, A. C., et al. 2009, *Nature*, 459, 540
- 2013, *MNRAS*, 429, 2917
- Fanali, R., Caccianiga, A., Severgnini, P., Della Ceca, R., Marchese, E., Carrera, F. J., Corral, A., & Mateos, S. 2013, *MNRAS*, 433, 648
- Gallimore, J. F., Baum, S. A., & O’Dea, C. P. 2004, *ApJ*, 613, 794
- Gallimore, J. F., Baum, S. A., O’Dea, C. P., & Pedlar, A. 1996, *ApJ*, 458, 136
- Gandhi, P., Horst, H., Smette, A., Hönig, S., Comastri, A., Gilli, R., Vignali, C., & Duschl, W. 2009, *A&A*, 502, 457
- Gandhi, P., et al. 2014, *ApJ*, 792, 117
- García, J., et al. 2014, *ApJ*, 782, 76
- Garmire, G. P., Bautz, M. W., Ford, P. G., Nousek, J. A., & Ricker, G. R. 2003, in *X-Ray and Gamma-Ray Telescopes and Instruments for Astronomy*. Edited by Joachim E. Truemper, Harvey D. Tananbaum. Proceedings of the SPIE, Volume 4851, pp. 28-44 (2003)., 28-44
- Gehrels, N., et al. 2004, *ApJ*, 611, 1005
- George, I. M. & Fabian, A. C. 1991, *MNRAS*, 249, 352
- George, I. M., Turner, T. J., Yaqoob, T., Netzer, H., Laor, A., Mushotzky, R. F., Nandra, K., & Takahashi, T. 2000, *ApJ*, 531, 52
- Goodman, A. A., Pineda, J. E., & Schnee, S. L. 2009, *ApJ*, 692, 91
- Grandi, P., et al. 1997, *A&A*, 325, L17
- Greenhill, L. J., Gwinn, C. R., Antonucci, R., & Barvainis, R. 1996, *ApJ*, 472, L21
- Groves, B. A., Cecil, G., Ferruit, P., & Dopita, M. A. 2004, *ApJ*, 611, 786
- Guainazzi, M., Molendi, S., Vignati, P., Matt, G., & Iwasawa, K. 2000, *New Astronomy*, 5, 235
- Guainazzi, M., et al. 1999, *MNRAS*, 310, 10
- Harrison, F. A., et al. 2013, *ApJ*, 770, 103
- Huchra, J. P., Vogeley, M. S., & Geller, M. J. 1999, *ApJS*, 121, 287
- Iwasawa, K., Fabian, A. C., & Matt, G. 1997, *MNRAS*, 289, 443
- Jaffe, W., et al. 2004, *Nature*, 429, 47
- Jansen, F., et al. 2001, *A&A*, 365, L1
- Kalberla, P. M. W., Burton, W. B., Hartmann, D., Arnal, E. M., Bajaja, E., Morras, R., & Pöppel, W. G. L. 2005, *A&A*, 440, 775
- Kallman, T., Evans, D. A., Marshall, H., Canizares, C., Longinotti, A., Nowak, M., & Schulz, N. 2014, *ApJ*, 780, 121
- Kaspi, S., et al. 2002, *ApJ*, 574, 643
- Kinkhabwala, A., et al. 2002, *ApJ*, 575, 732
- Koshida, S., et al. 2014, *ApJ*, 788, 159
- Kraemer, S. B. & Crenshaw, D. M. 2000, *ApJ*, 544, 763
- Kraemer, S. B., Ruiz, J. R., & Crenshaw, D. M. 1998, *ApJ*, 508, 232
- Krolik, J. H. & Kriss, G. A. 1995, *ApJ*, 447, 512
- Kuo, C. Y., et al. 2011, *ApJ*, 727, 20
- Lada, C. J., Alves, J., & Lada, E. A. 1999, *ApJ*, 512, 250
- Lansbury, G. B., et al. 2014, *ApJ*, 785, 17
- Lightman, A. P. & White, T. R. 1988, *ApJ*, 335, 57
- Lodato, G. & Bertin, G. 2003, *A&A*, 398, 517
- Lombardi, M., Lada, C. J., & Alves, J. 2010, *A&A*, 512, A67
- López-Gonzaga, N., Jaffe, W., Burtscher, L., Tristram, K. R. W., & Meisenheimer, K. 2014, *A&A*, 565, A71
- Macchetto, F., Capetti, A., Sparks, W. B., Axon, D. J., & Boksenberg, A. 1994, *ApJ*, 435, L15
- Magdziarz, P. & Zdziarski, A. A. 1995, *MNRAS*, 273, 837
- Markowitz, A., Papadakis, I., Arévalo, P., Turner, T. J., Miller, L., & Reeves, J. N. 2007, *ApJ*, 656, 116
- Markowitz, A., Reeves, J. N., George, I. M., Braitto, V., Smith, R., Vaughan, S., Arévalo, P., & Tombesi, F. 2009, *ApJ*, 691, 922
- Markowitz, A., et al. 2003, *ApJ*, 593, 96
- Marshall, H. L. 2012, in *Society of Photo-Optical Instrumentation Engineers (SPIE) Conference Series*, vol. 8443 of *Society of Photo-Optical Instrumentation Engineers (SPIE) Conference Series*, 1
- Martins, L. P., Rodríguez-Ardila, A., de Souza, R., & Gruenewald, R. 2010, *MNRAS*, 406, 2168
- Matt, G., Bianchi, S., Guainazzi, M., & Molendi, S. 2004, *A&A*, 414, 155
- Matt, G., Fabian, A. C., Guainazzi, M., Iwasawa, K., Bassani, L., & Malaguti, G. 2000, *MNRAS*, 318, 173
- Matt, G., et al. 1997, *A&A*, 325, L13
- McHardy, I. M., Gunn, K. F., Uttley, P., & Goad, M. R. 2005, *MNRAS*, 359, 1469
- McHardy, I. M., Koerding, E., Knigge, C., Uttley, P., & Fender, R. P. 2006, *Nature*, 444, 730
- McHardy, I. M., Papadakis, I. E., Uttley, P., Page, M. J., & Mason, K. O. 2004, *MNRAS*, 348, 783
- Miller, J. S., Goodrich, R. W., & Mathews, W. G. 1991, *ApJ*, 378, 47
- Molinari, S., et al. 2011, *ApJ*, 735, L33
- Murphy, K. D. & Yaqoob, T. 2009, *MNRAS*, 397, 1549
- Nandra, K., O’Neill, P. M., George, I. M., & Reeves, J. N. 2007, *MNRAS*, 382, 194
- Nandra, K., et al. 2013, arXiv, 1306.2307, 1306.2307
- Nandra, P. 2014, in *The X-ray Universe 2014*, edited by Jan-Uwe Ness. id.10
- Nejkova, M., Sirocky, M. M., Nikutta, R., Ivezić, Ž., & Elitzur, M. 2008, *ApJ*, 685, 160
- Nevalainen, J., David, L., & Guainazzi, M. 2010, *A&A*, 523, A22
- Ogle, P. M., Brookings, T., Canizares, C. R., Lee, J. C., & Marshall, H. L. 2003, *A&A*, 402, 849
- Oliva, E., et al. 2001, *A&A*, 369, L5
- Parker, M. L., et al. 2014, *MNRAS*, 443, 1723
- Perri, M., Puccetti, S., Spagnuolo, N., Davis, K., A. Forster, Grefenstette, B., Harrison, F., & Madsen, K. 2014, *The NuSTAR Data Analysis Software Guide*, http://heasarc.gsfc.nasa.gov/docs/nustar/analysis/nustar_swguide.pdf, v1.7 ed.
- Petrucchi, P. O., et al. 2001, *ApJ*, 556, 716
- Pound, M. W. 1998, *ApJ*, 493, L113
- Raban, D., Jaffe, W., Röttgering, H., Meisenheimer, K., & Tristram, K. R. W. 2009, *MNRAS*, 394, 1325
- Ramos Almeida, C., et al. 2009, *ApJ*, 702, 1127
- Rana, V., et al. 2014, *ArXiv e-prints*, 1401.4637
- Reeves, J. N. & Turner, M. J. L. 2000, *MNRAS*, 316, 234
- Risaliti, G., et al. 2009, *ApJ*, 696, 160
- Ross, R. R. & Fabian, A. C. 2005, *MNRAS*, 358, 211
- Schartmann, M., Burkert, A., Krause, M., Camenzind, M., Meisenheimer, K., & Davies, R. I. 2010, *MNRAS*, 403, 1801
- Shemmer, O., Brandt, W. N., Netzer, H., Maiolino, R., & Kaspi, S. 2006, *ApJ*, 646, L29
- Suganuma, M., et al. 2006, *ApJ*, 639, 46
- Swartz, D. A., Ghosh, K. K., Tennant, A. F., & Wu, K. 2004, *ApJS*, 154, 519
- Tremblin, P., et al. 2014, *A&A*, 564, A106
- Tsujimoto, M., et al. 2011, *A&A*, 525, A25
- Tully, R. B. 1988, *Nearby galaxies catalog* (Cambridge University Press)
- Unger, S. W., Lewis, J. R., Pedlar, A., & Axon, D. J. 1992, *MNRAS*, 258, 371
- Urry, C. M. & Padovani, P. 1995, *PASP*, 107, 803
- Veilleux, S., Shopbell, P. L., Rupke, D. S., Bland-Hawthorn, J., & Cecil, G. 2003, *AJ*, 126, 2185
- Verner, D. A., Ferland, G. J., Korista, K. T., & Yakovlev, D. G. 1996, *ApJ*, 465, 487
- Walton, D. J., Roberts, T. P., Mateos, S., & Heard, V. 2011, *MNRAS*, 416, 1844
- Walton, D. J., et al. 2013, *ApJ*, 779, 148
- 2014, *ArXiv e-prints*, 1402.2992
- Wik, D. R., et al. 2014, *ArXiv e-prints*, 1403.2722
- Wilms, J., Allen, A., & McCray, R. 2000, *ApJ*, 542, 914
- Wilson, A. S. & Ulvestad, J. S. 1987, *ApJ*, 319, 105
- Wise, M. W., Huenemoerder, D. P., & Davis, J. E. 1997, in *Astronomical Data Analysis Software and Systems VI*, eds. G. Hunt & H. Payne, vol. 125 of *Astronomical Society of the Pacific Conference Series*, 477
- Woo, J.-H. & Urry, C. M. 2002, *ApJ*, 579, 530
- Yaqoob, T. 2012, *MNRAS*, 423, 3360
- Yaqoob, T. & Padmanabhan, U. 2004, *ApJ*, 604, 63, astro-ph/0311551
- Young, A. J., Wilson, A. S., & Shopbell, P. L. 2001, *ApJ*, 556, 6